# Towards an improved understanding of the impact of clouds and precipitation on the representation of aerosols over the Boreal **Forest in GCMs**

- Sini Talvinen<sup>1,\*</sup>, Paul Kim<sup>2</sup>, Emanuele Tovazzi<sup>2</sup>, Eemeli Holopainen<sup>1,3,#</sup>, Roxana Cremer<sup>4,\$</sup>, Thomas 5
- Kühn<sup>5</sup>, Harri Kokkola<sup>1,3</sup>, Zak Kipling<sup>6</sup>, David Neubauer<sup>7</sup>, João C. Teixeira<sup>8</sup>, Alistair Sellar<sup>8</sup>, Duncan Watson-Parris<sup>9</sup>, Yang Yang<sup>10</sup>, Jialei Zhu<sup>11</sup>, Srinath Krishnan<sup>12</sup>, Annele Virtanen<sup>1</sup> and Daniel G. 7
- Partridge<sup>2</sup> 8

3 4

- <sup>1</sup>Department of Technical Physics, University of Eastern Finland, Kuopio, 70210, Finland 10
- 11 <sup>2</sup>Department of Mathematics and Statistics, University of Exeter, Exeter, EX4 4QF, United Kingdom
- 12 <sup>3</sup>Atmospheric Research Centre of Eastern Finland, Finnish Meteorological Institute, Kuopio, 70211, Finland
- <sup>4</sup>Department of Environmental Science, Stockholm University, Stockholm, 106 91, Sweden 13
- Weather and Climate Change Impact Research, Finnish Meteorological Institute, Helsinki, 00101, Finland 14
- 15 <sup>6</sup>European Centre for Medium-Range Weather Forecasts, Reading, RG2 9AX, United Kingdom
- <sup>7</sup>Institute for Atmospheric and Climate Science, ETH Zürich, Zurich, Switzerland 16
- <sup>8</sup>Met Office Hadley Centre, Exeter, EX1 3PB, United Kingdom 17
- Scripps Institution of Oceanography and Halicioğlu Data Science Institute, University of California San Diego, La Jolla, 18
- 19 CA 92093. United states
- <sup>10</sup>School of Environmental Sciences and Engineering, Nanjing University of Information Science and Technology, 20
- Nanjing, Jiangsu, China
- 21 22 <sup>11</sup>Institute of Surface-Earth System Science, School of Earth System Science, Tianjin University, Tianjin, 300072, China
- 23 12CICERO Center for International Climate Research, Oslo, 0349, Norway
- 24 25 \*now at Department of Environmental Science and Bolin Centre for Climate Research, Stockholm University, Stockholm, 10691. Sweden
- 26 \*now at Institute for Chemical Engineering Sciences of Foundation for Research and Technology Hellas, Patras, 26504,
- 27 Greece
- 28 \$now at Leibniz Institute for Tropospheric Research, Leipzig, 04318, Germany 29
- 30 Correspondence to: sini.talvinen@aces.su.se, D.G.Partridge@exeter.ac.uk

#### 31 Abstract

34

42.

- 32 General circulation models (GCMs) face uncertainties in estimating Earth's radiative budget due to aerosol cloud
- 33 interactions (ACI). Accurate aerosol number size distributions are crucial for improving ACI representation in GCMs,
  - requiring precise modelling of aerosol source and sink processes throughout their lifetime. This study employs a Lagrangian trajectory framework to analyse how clouds and precipitation influence aerosol lifecycles during transport in
- 35
- 36 the boreal forest. A comparison of two GCMs, the United Kingdom Earth System Model (UKESM1) and ECHAM6.3-
- 37 HAM2.3 MOZ1.0 with the SALSA2.0 aerosol module (ECHAM-SALSA), is conducted. An evaluation against in situ 38
- observations and reanalysis based trajectories is performed. Results show that overall aerosol precipitation trends are 39
- similar between GCMs and observations. However, seasonal differences emerge: in summer, UKESM1 exhibits more 40 efficient aerosol removal via precipitation than ECHAM-SALSA and observations, whereas in winter, the opposite is
- 41 observed. These were found to coincide with differences in key variables controlling aerosol activation, such as sub-grid
  - scale updraughts and number size distributions. For example, in winter the removal of the total aerosol mass in ECHAM-
- 43 SALSA was stronger compared to UKESM1, coinciding with higher activated fractions during airmass transport, which,
- 44 on the other hand, were likely due to the larger sub-grid scale updraughts in ECHAM SALSA. For both GCMs,
- 45 investigation of aqueous phase chemical processing along the trajectories showed clear increase of SO4 mass for cloud-

processed air masses when compared to clear sky conditions, in line with the observations. As expected, based on the model parametrizations, these increases in SO4 were mostly distributed to the accumulation mode aerosols. Global climate models (GCMs) face uncertainties in estimating Earth's radiative budget due to aerosol-cloud interactions (ACI). Accurate particle number size distributions (PNSDs) are crucial for improving ACI representation, requiring precise modelling of aerosol sources and sinks. Using a Lagrangian trajectory framework, we examine how clouds and precipitation influence aerosols during transport, and thereby influence aerosol-cloud relationships in the boreal forest. Two GCMs, the United Kingdom Earth System Model (UKESM1) and ECHAM6.3-HAM2.3-MOZ1.0 with the SALSA2.0 aerosol module (ECHAM-SALSA), are complemented with model-derived trajectories and evaluated against in-situ observations, which are accompanied by reanalysis trajectories. Overall aerosol-precipitation trends are similar between GCMs and observations. However, seasonal differences emerge: in summer, UKESM1 exhibits more efficient aerosol removal via precipitation than ECHAM-SALSA and observations, whereas in winter, the opposite is observed. These differences coincide with key variables controlling aerosol activation, such as sub-grid scale updraught velocities and PNSDs. For example, in winter, removal of total aerosol mass in ECHAM-SALSA was stronger than in UKESM1, coinciding with higher activated fractions and larger sub-grid scale updraught velocities in ECHAM-SALSA. For both GCMs, cloud processing along trajectories increased SO4 mass, mainly in the accumulation mode, consistent with observations and model parametrizations. Discrepancies arise more from differences in PNSDs and updraught velocities than from wet removal parametrizations, an example being the underrepresentation of small particles in UKESM1. While our findings are representative of boreal region with predominantly stratiform precipitation, further work is needed to evaluate their applicability to other regions.

46

47

48

49

50

51

52

53

54

55

56

57

58

59

60

61

62

63

64

65

#### 1 Introduction

Atmospheric aerosol particle concentrations are influenced by their sources and sinks which affect their lifetimes in the atmosphere, and also play a significant role in our climate system through different mechanisms. One of the most important mechanisms are aerosol-cloud interactions (ACI), which are still causing the largest uncertainties on the effects of aerosols on Earth's radiative budget in general circulationglobal climate models (GCMs, Boucher, 2013; Watson-Parris et al., 2019; Bellouin et al., 2020; Forster et al., 2021), and therefore partly masking the warming effect by greenhouse gases (Bauer et al., 2022; Quaas et al., 2022). It is critical, therefore, that the microphysical processes influencing ACIs are well understood and accurately modelled. To accurately simulate ACI in GCMs, the aerosol number size distributions need to be correctly described (e.g., Mann et al., 2010). <u>Traditionally, discrepancies in particle size distributions between</u> observations and models exceed those between modal and sectional approaches, with sectional methods dividing the distribution into discrete size binsTraditionally, the differences in particle size distributions between observations and models are larger than the differences between modal and sectional approaches (Mann et al., 2012). However, but larger differences in concentrations may emerge when chemistry of the aerosols is inspected (Laakso et al., 2022). On the other hand, to accurately represent the aerosol number size distributions, GCMs also need to accurately represent the source and sink processes that act on the aerosol during its lifetime and transport in the atmosphere. The impact of precipitation on the evolution of the size distribution is very important (e.g., Browse et al., 2014; Khadir et al., 2023), but remains a major uncertainty in the GCMs. Often, when GCM parametrizations are assessed the models are evaluated against observations or other GCMs by inspecting differences in averages of variables (or relationships between multiple variables) over certain time spans (e.g., Blichner et al., 2024; Gliß et al., 2021; Labe and Barnes, 2022; Maher et al., 2021; Pathak et al., 2023) in a Eulerian perspective. However, GCM evaluations in which the evolution of aerosols and other variables is followed over both time and space in more detail using GCM Lagrangian trajectory-based evaluation frameworks that have have been recently introduced in recent years (e.g., Kim et al., 2020). Such frameworks facilitate pave the way for the development of more rigorous observational constraints on uncertain physical and chemical aerosol processes for GCM evaluation, by including temporal and spatial information associated with the air-mass history.

ACIs include scavenging of aerosol particles by precipitation, cloud droplets and ice crystals. Wet scavenging is one of the most efficient removal routes of particles from the atmosphere (e.g., Ohata et al., 2016; Liu et al., 2020). Wet scavenging of aerosol particles can be further divided into in-cloud scavenging and below cloud scavenging. Wet scavenging via in-cloud scavenging involves the loss of aerosol particles when they become activated into cloud droplets or ice crystals (nucleation scavenging) which can then further collide with interstitial aerosols in-cloud (e.g., Ohata et al., 2016; Seinfeld and Pandis, 2016). Below-cloud scavenging concerns the removal of aerosol by rainfall from the collection of particles due to collisions with falling raindrops and snow and ice from precipitation (e.g., Ohata et al., 2016). Current understanding identifies the contribution of in-cloud scavenging, followed by removal via precipitation to be, on average, the most important sink globally for accumulation mode particles (particle diameter  $d_p \sim 100$ -1000 nm). Ultrafine ( $d_p < 100$  nm) and coarse particles ( $d_p > 1$  µm), on the other hand, are more efficiently removed by below-cloud scavenging (e.g., Andronache, 2003; Textor et al., 2006; Croft et al., 2009; Ohata et al., 2016). In addition to wet scavenging, clouds can also alter the particle properties through aqueous phase oxidation processes. For example, sulfate production due to oxidation of gaseous sulfur dioxide inside clouds is considered as one of the most important mass addition processes for sulfate (e.g., Ervens, 2015 and references therein). Production of organics through aqueous phase processes has also been reported in some environments (e.g., Ervens et al., 2018; Lamkaddam et al., 2021).

Investigation of the effects of precipitation and clouds has traditionally been Eulerian, in which local estimates of precipitation are employed (e.g., Wang et al., 2021). Lagrangian approaches, in which air mass trajectories are exploited to examine the effects of precipitation on aerosols and their composition as the air masses travel to the receptor location, have, however, increased in popularity during the recent years (Dadashazar et al., 2021; Heslin-Rees et al., 2024; Isokääntä et al., 2022; Kesti et al., 2020; Khadir et al., 2023; Tunved et al., 2004, 2013; Tunved and Ström, 2019). These types of studies can provide significantly more detailed insights by considering the interplay between aerosols, clouds and precipitation during airmassair massair massair massair shistory, that cannot be achieved using Eulerian approaches. All these studies investigated how the total accumulated precipitation experienced along air-mass trajectories derived from reanalysis data affects a particle size distribution measured at a specific receptor site. Tunved et al. (2013), for example, investigated aerosols in the Arctic (Zeppelin station, Ny-Ålesund, Norway) and observed strong removal of sub-micron particulate mass up to 10 mm of accumulated precipitation. They suggested the in-cloud scavenging (followed by removal via precipitation) is the dominant removal pathway, as larger particles showed first a decrease in their concentration as a function of accumulated precipitation during transport, followed by the removal smaller sizes. Kesti et al. (2020) studied aerosols at the humid tropical monsoon climate in the Maldives, and observed more efficient removal on the number concentration of the accumulation mode particles with increasing accumulated precipitation, when compared to the smaller particle sizes. Dadashazar et al. (2021) studied sub-tropical environments in Bermuda and concluded that PM2.5 mass experienced the strongest sensitivity to accumulated precipitation up to 5 mm whereas precipitation exceeding this limit had no major effects on the particulate mass. Khadir et al. (2023) further reported that precipitation can, in some instances, serve as a source of aerosols.

105

106

107

108

109

110

111

112

113

114

115

116

117

118

119

120

121

122

123

124

125

126

127

128

129

130

131

132

133

134

135

136

137

138

139

140

141

142

143 144 In addition to the effects of precipitation for aerosols in Scandinavian boreal region, a previous study by Isokääntä et al. (2022) used relative humidity (>94%) as a proxy for in-cloud exposure in boreal air masses and found a pronounced increase in sulfate mass in air masses recently influenced by non-precipitating clouds, while no significant aqueous-phase production of organic aerosol was observed—likely due to dominant gas-phase biogenic sources, investigated the incloud aqueous phase processing of aerosol in more detail by using relative humidity as a proxy to estimate the cloudiness along the air masses (Isokääntä et al., 2022). This study observed a significant increase in sulfate mass in air masses that had recently been in non-precipitating clouds compared to air masses that had not experienced wet processing during the last 24 hours. Isokääntä et al. (2022) didn't observe, however, significant aqueous phase production of organic mass, likely due to the environment studied (boreal forest), in which production of organics from biogenic sources via gas-phase chemistry is dominating. This is in line with earlier observations made for boreal region consistent with findings from in central Sweden (Graham et al., 2020). The effects of total precipitation were studied by Khadir et al. (2023) in three different environments, including tropical forest, arctic marine and boreal forest. They concluded the effects of more recent precipitation differ from those taking place further away from the receptor site. They also showed that these effects were dependent on the particle size and receptor site (influenced by e.g., the type of precipitation, stratiform vs convective). Increased removal via precipitation has also been shown to lead to long-term reductions in absorbing aerosols in the Arctic (Heslin Rees et al., 2024). These earlier results suggest that sulfate may be more strongly affected by cloud processing and wet removal than organic aerosol, with removal efficiency likely influenced by factors such as precipitation timing, aerosol type, and the stage of the air mass trajectory. Our study builds on this by exploring these aspects across multiple models and observations, employing the The GCM Lagrangian evaluation framework presented by Kim et al. (2020). With this framework in which airmassair mass trajectories can be obtained from global GCM simulations. This is achieved by eollocatco-locating multiple variables (for example, aerosol size distribution and 145 chemical composition) from the GCMs to the airmassair mass trajectories calculated from the GCM meteorological data 146 (Kim et al., 2020). This methodology allows us to transparently evaluate and compare the wet scavenging and aqueous-147 phase processing between the observations and GCMs within the Lagrangian trajectory framework in unprecedented 148 detail. thus gives the possibility to extend the type of Lagrangian analysis performed in the aforementioned studies to 149 transparently evaluate and investigate aerosol properties and processes during transport in climate models. 150 All the studies discussed above inspected the total precipitation (rain and snow) originating from stratiform (often also 151 called "large scale") and convective clouds. Stratiform precipitation dominates in mid- and northern latitudes (30-60° 152 from the equator and poleward), whereas the tropics are usually associated with strong convective conditions (e.g., 153 Schumacher and Funk, 2023). Therefore, as our study is mostly focused on the boreal forest area in northern Europe, our 154 focus is on stratiform precipitation. The diverging effects of different precipitation types on aerosols was also pointed out 155 by Khadir et al. (2023) as they observed recent precipitation in the tropics (i.e., mostly convective precipitation) can be 156 associated with downdrafts providing a source for small particles by transporting them to the boundary layer from higher 157 altitudes (see e.g., Franco et al., 2022; Machado et al., 2021; McCoy et al., 2021; Williamson et al., 2019). 158 In this work, the effects of wet processing (wet removal and aqueous phase processing) along air mass trajectories on 159 modelled aerosol size distributions are compared with long term observations of aerosol size distributions in Hyytiälä, 160 Finland. The observations are combined with ERA Interim reanalysis trajectories, and the trajectories to be utilized with 161 the GCM variables are calculated with the GCM simulation (nudged to ERA Interim reanalysis) output meteorology. For 162 obtaining airmass trajectories, a variety of options exists with the most commonly used being the FLEXible PARTicle 163 dispersion model (FLEXPART; Pisso et al., 2019) and The Hybrid Single Particle Lagrangian Integrated Trajectory 164 model (HYSPLIT; Draxler and Hess, 1998; Stein et al., 2015). Both can be run either in forward or backward mode, and 165 in this study, HYSPLIT is employed to obtain backward air mass trajectories for our receptor site in the boreal forest area 166 for a period from the beginning of 2005 to the end of 2018. 167 This study compares the effects of wet processing (wet removal and aqueous-phase processing) on modelled aerosol size 168 distributions with long-term observations from Hyytiälä, Finland. Observational trajectories are based on ERA-Interim 169 reanalysis, while model trajectories are calculated using meteorology data from GCM AMIP-style simulations in which 170 wind fields were nudged to ERA-Interim. The GCMs used in this study include UKESM1 (United Kingdom Earth System 171 Model, e.g., Sellar et al., 2019) and ECHAM6.3-HAM2.3-MOZ1.0 with sectional aerosol module SALSA2.0 (hereafter 172 ECHAM-SALSA, Stevens et al., 2013; Kokkola et al., 2018; Tegen et al., 2019). Both GCMs are part of the Aerosol 173 Comparisons between Observations and Models (AeroCom) Phase III GCM Trajectory Experiment (GCMTraj) in which 174 a comparison between the GCMs against reanalysis meteorology was conducted for the years between 2009 and 2013. In 175 this study, to facilitate even more robust comparison to observations, the simulations for UKESM1 and ECHAM-SALSA 176 were extended to cover the years from 2005 to 2018 which are also available from the observations. Comparison between 177 modal (UKESM1) and sectional (ECHAM-SALSA) approaches for estimating the aerosol microphysics provides 178 additional insight into the model behaviour via this Lagrangian evaluation approach. The Hybrid Single-Particle 179 Lagrangian Integrated Trajectory model (HYSPLIT; Draxler and Hess, 1998; Stein et al., 2015) is employed to obtain the 180 backward air mass trajectories. A key difference between our study and previous work, including Isokääntä et al. (2022), 181 is our focus on stratiform precipitation rather than total precipitation. Stratiform precipitation is the dominant type in mid-

and high-latitude regions (30-60° from the equator and poleward), whereas tropical regions are typically influenced by

182

183

linked to downdrafts that transport small particles from higher altitudes to the boundary layer (see also Franco et al., 2022)
Machado et al., 2021; McCoy et al., 2021; Williamson et al., 2019).
For the GCMs, the Lagrangian framework, similar as presented in Isokääntä et al., (2022), is further extended by the
newly developed approach mentioned above to govern more parameters than usually available from typical back-
trajectory models. This is achieved by collocatco-locating multiple variables (for example, acrosol size distribution and
chemical composition) from the GCMs to the airmassair mass trajectories (Kim et al., 2020). This methodology allows
us to transparently evaluate and compare the wet seavenging and aqueous-phase processing between the observations and
GCMs within the Lagrangian trajectory framework in unprecedented detail.
The aim of our research can be summarized into two main objectives (1-2) including two additional research questions (a-b):
1. Do the relationships between aerosols and experienced precipitation during transport differ between the
measurements and GCMs and what are the drivers for the observed differences?
a. How representative are UKESM1 and ECHAM SALSA compared to other GCMs that participated in
the AeroCom GCMTraj experiment?
b. Is the precipitation at the surface representative of describing the experienced precipitation by the air mass?
2. Do the GCMs exhibit similar increase in sulfate mass due to in-cloud production as the observations and are the observed effects reasonable when reflected to model parametrizations?
We start out investigation in Sect. 2 by first introducing the observational datasets, followed by summarising the GCM
simulations along with details on the air mass trajectory calculations and data co-locations employed in this work. The

aerosol properties at SMEAR II are given in Sect. 3 as a necessary background for the following Lagrangian analysis.

The relationships between precipitation and aerosol mass and number in the Lagrangian framework are presented first

(Sect. 4.1-4.3), followed by a process-chain type evaluation (Sect. 4.4) to understand the driving forces in the

relationships. Finally, in Sect. 5, the effects of aqueous-phase processing are presented, followed by overall conclusions

northern Europe, stratiform precipitation is most relevant. The differing impacts of precipitation types on aerosols have

also been highlighted by Khadir et al. (2023), who showed that recent tropical precipitation—largely convective—can be

(Sect. 6) and outlook (Sect. 7).

Formatted: Normal, Indent: Left: 1,9 cm, No bullets or numbering

#### 2 Data and methods

211

212

223

224

225

226

233

234

235

236

237

238

239

240

241

242

243

244

245

246

247

248

#### 2.1 Observations at SMEAR II

213 Observational data used in this study include long-term measurements of aerosol number size distributions and particle 214 chemistry from SMEAR II (Station for Measuring Ecosystem-Atmosphere Relations in; Hari and Kulmala, 2005) and are 215 described in detail in Isokääntä et al. (2022) and the references therein. SMEAR II station (Hyytiälä, Finland) is classified 216 as a rural environment, surrounded by relatively homogenous Scots pine (Pinus sylvesteris) forest. In this work particle 217 number size measurements (covering particle diameters between 3-1000 nm) obtained with a differential mobility particle 218 sizer (DMPS, e.g., Aalto et al., 2001) are utilized. Chemical composition (organics, sulfate, and equivalent black carbon) 219 of the particles in the sub-micron range were derived from an aethalometer (e.g., Drinovec et al., 2015) and aerosol 220 chemical speciation monitor (ACSM, Ng et al., 2011). The dataset for particle number size measurements spans 2005-221 2018, slightly shorter than in Isokääntä et al. (2022), to match the GCM simulation period. -The ASCM data extends from 222 2012 to 2018. The dataset used in this study is reduced compared to Isokääntä et al. (2022) and extends to the end of 2018

### 2.2 Summaries of the GCMs used in this study

to facilitate comparisons to the simulation period of the GCMs.

## 2.2.1 UKESM1

components following the protocol set by the Atmospheric Model Intercomparison Project (AMIP, Eyring et al., 2016).

The atmospheric component of the model The science configuration of the atmosphere component is based on the Global Atmosphere 7.1 (GA7.1) and the Global Land 7.0 (GL7.0) configurations, as described by Walters et al. (2019), used in the configurationThese are part of the Hadley Centre Global Environment Model version 3 (HadGEM3; Hewitt et al., 2011), which is coupled to the terrestrial carbon/nitrogen cycles (Sellar et al., 2019). It—and includes interactive stratosphere—troposphere chemistry from the (Archibald et al., 2020) from the UK Chemistry and Aerosol (UKCA) model

(UKCA; (Archibald et al., 2020; Morgenstern et al., 2009; O'Connor et al., 2014)-model.

of DMS and primary marine organic aerosol (Mulcahy et al., 2020).

The United Kingdom Earth System Model (UKESM1) configuration used in this study uses the atmospheric and land

(2017) and horizontally interpolated to the model resolution. In this setup, the dynamic vegetation model (Cox, 2001) is turned off. Instead, prescribed vegetation from a historical coupled UKESM1 simulation is used to maintain consistent land-use forcing between the coupled and AMIP experiments. In this model setup, the dynamic vegetation model (Cox, 2001) is deactivated and replaced by prescribed vegetation properties from a coupled historical simulation with the same base model to preserve consistency in the forcing due to land use change between the UKESM1 coupled and AMIP experiments. In a similar fashion, seawater concentrations of dimethyl sulfide (DMS) and chlorophyll-a monthly climatologies are taken from the coupled historical experiment and are used by the atmosphere model top calculates fluxes

Following the AMIP protocol, sea surface temperature and sea ice are taken from the unmodified dataset of Durack et al.

In addition, tThe simulations used in this study were nudged to ERA-Interim reanalysis (Dee et al., 2011; Telford et al., 2008) u/v (horizontal and vertical), wind fields and surface pressure following the setup design for the AeroCom GCMTraj phase III experiment. The model resolution for these configurations was 1.875° × 1.25° longitude—latitude, which corresponds corresponding to a horizontal resolution of approximately 135 km in the midlatitudes. The model has 85 vertical levels which are divided such that 50 levels are between 0 and 18 km and the remaining 35 levels cover heights between 18 and 85 km.

Field Code Changed

Formatted: English (United States)

Atmospheric composition within UKESM1 is implemented as part of the United Kingdom Chemistry and Aerosol (UKCA) model, (e.g., Archibald et al., 2020). Within UKCA, the Global Model of Aerosol Processes (GLOMAP; Mann et al., 2010; Mulcahy et al., 2020) is used. This scheme simulates multicomponent global aerosols, including, for example, sulfate, black carbon, and organic matter. The aerosol particle size distribution is represented using five log-normal modes, nucleation soluble, Aitken soluble, accumulation soluble, coarse soluble and Aitken insoluble visualized in Figure S1. More details, including the size ranges for each aerosol mode, are presented in Sect. S1.1. The GLOMAP model also includes various microphysical processes that affect the evolution of aerosol properties. Wet scavenging processes in UKESM1, including below-cloud (impaction), in-cloud (nucleation) and plume scavenging are summarized in Sect. S2 and references therein. As a key difference to ECHAM-SALSA (Sect. 2.2.2) concerning the aerosol parametrizations, new particle formation in the boundary layer is not yet implemented in UKESM1 (Mulcahy et al., 2020).

For this study the AeroCom GCMTraj UKESM1 simulations (2009-2013) were extended\_ran longer to cover years from 2005 to 2018 to facilitate robust statistical comparison with the aerosol size distributions and composition measurements obtained from SMEAR II. The model output fields were extracted at high temporal resolution (3-hourly output) for all model levels (when available, otherwise noted as surface). The diagnostics fields utilized in this work (see also Table S4) are aerosol particle size distribution variables (number concentrations and dry diameters for each aerosol mode), chemical components including mass mixing ratios of sulfate noted here as SO<sub>4</sub> (extracted as sulfuric acid H<sub>2</sub>SO<sub>4</sub> and then converted, see Sect. S1.1), organic matter (noted here as OA) and black carbon (BC), total (including both liquid rain and snow) stratiform and convective precipitation at the surface, dry air density, sub-grid scale updraught velocity, number of activated particles, total precipitation at the surface, relative humidity and cloud fractions. Additionally, from UKESM1, wet scavenging coefficients (representing removal within the whole atmospheric column) for the different removal processes (nucleation, impaction and plume) and species (OA, H<sub>2</sub>SO<sub>4</sub> and BC), SO<sub>2</sub> concentrations, and both vertically resolved and surface liquid stratiform precipitation are inspected. These variables and/or variables derived from them are eollocated to the UKESM1 derived HYSPLIT back-trajectories as described in Sect. 2.3.

### 2.2.2 ECHAM-SALSA

 circulation model ECHAM (Stevens et al., 2013) coupled with the Hamburg Aerosol Model HAM (Tegen et al., 2019) and chemistry model MOZ (Schultz et al., 2018). For this work, as for UKESM1, simulations follow AMIP style runs following the AeroCom phase III GCMTraj experiment setup. Therefore, as for UKESM1, the u/v wind fields and surface pressure were nudged towards ERA-Interim reanalysis data. In addition, the sea surface temperature and sea ice cover were prescribed based on monthly mean climatologies obtained from the AMIP project (Eyring et al., 2016). The model solves atmospheric circulation with vertical gridding of 47 layers extending roughly up to 80 km. Model horizontal resolution for these configurations is  $1.875^{\circ} \times 1.875^{\circ}$  longitude—latitude.

ECHAM6.3-HAM2.3-MOZ1.0 is a global aerosol-chemistry-climate model consisting of the atmospheric general

ECHAM6.3-HAM2.3-MOZ1.0 is paired with the sectional aerosol microphysics model SALSA2.0 (ECHAM-SALSA) in which the size distribution is divided into 3 subranges ( $d_{p1} = 3 - 50$  nm,  $d_{p2} = 50 - 700$  nm and  $d_{p3} = 700$  nm - 10 µm) including 10 size classes in logarithmical size space. Subranges  $d_{p2}$  and  $d_{p3}$  include parallel size classes for insoluble and soluble aerosol species, making the total number of size classes 17 (Kokkola et al., 2018), visualized in Figure S1. More details of the subranges and their compositions are given in Sect. S1.2. Additional details of the aerosol processes calculated in SALSA2.0 can be found in Kokkola et al. (2018) and Holopainen et al. (2020). Wet scavenging parametrizations are summarized in Sect. S2 for below- and in-cloud scavenging.

As for UKESM1, simulations cover the years from 2005 to 2018 for ECHAM-SALSA. Data output—from ECHAM-SALSA is also 3-hourly and vertically resolved unless the variable is noted as surface variable. The diagnostics extracted from ECHAM-SALSA—for this study (see also Table S4) include aerosol particle size distribution variables (number concentrations and dry diameters for each size class), chemical components including mass mixing ratios of sulfate (SO<sub>4</sub>), organics (noted here as OA) and black carbon (BC), total (including both liquid rain and snow) stratiform and convective precipitation at the surface, dry air density, sub-grid scale updraught velocity, number of activated particles, total precipitation at the surface, relative humidity and cloud fractions. Similar to UKESM1, these variables and/or variables calculated from them are eollocated to the ECHAM-SALSA derived HYSPLIT back-trajectories as described in Sect. 2.3.

## 2.3 Airmass Air mass trajectory calculations and data collocat co-location

#### 2.3.1 HYSPLIT

2015) model for the period from January 2005 to December 2018. The 4-day long back trajectories were used to ensure consistency with the results from Isokääntä et al. (2022). In addition, this is typically a long enough period for slowly moving air masses to travel to the boreal environment from high arctic and marine areas. Arrival height of the trajectories to the receptor station was set to 100 m above the ground level. To obtain the GCM derived trajectories, the meteorological fields from the GCMs were first converted into a consistent netCDF4 format which was then converted into the ARL packed HYSPLIT4 compatible format (Kim et al., 2020). For this study, and for the AeroCom GCM Trajectory Experiment tThe GCM and ERA-Interim (Dee et al., 2011) reanalysis meteorological datasets required for the HYSPLIT4 trajectory calculations were re-gridded to a consistent 1° horizontal resolution. The vertical discretization of the GCM variables was provided on terrain-following model levels for those GCMs that have their native output as hybrid sigma-pressure levels. In UKESM1, however, the native output is on hybrid height levels, which is not supported by HYSPLIT. Therefore, UKESM1 was output on fixed pressure levels instead, which were selected to closely match the ERA-Interim pressure levels.

The 4-day (96 h) back trajectories arriving at SMEAR II were calculated by version 5.1.0 of the HYSPLIT (Stein et al.,

Trajectories were calculated for every 3<sup>rd</sup> hour for both reanalysis data and the GCMs, which was also the usedcorresponding to GCM-simulation diagnostic output resolution. This led to 8 trajectories per day, a total of 40896 air mass trajectories between 2005-2018 before applying any pre-processing and temporal harmonization of the data (Sect. 2.4). Hereafter, when discussing observational data coupled with the ERA-Interim back-trajectories, those are referred as observations unless mentioned otherwise. It should be noted that reanalysis data is not interchangeable with observations but is used as a proxy in this study.

## 2.3.2 Collocat Co-location of GCM data along the airmassair mass trajectories

vertically (variables which covered different model or pressure levels) eollocatco-located to the GCM derived airmassair mass trajectories. In short, a eollocatco-locator tool (Kim et al., 2020) based off the Community Intercomparison Suite (CIS, Watson-Parris et al., 2016) was used to eollocatco-locate 4-dimensional data which uses hybrid altitude coordinates. As the default interpolator within CIS has often difficulties eollocatco-locating to the near-surface trajectory points (due to surrounding grid-boxes being at the boundaries of the data domain), our-the modified eollocatco-locator provided more flexibility for the interpolation of these near-surface points. This is relevant also in this work, as for our surface sites the

The variables from the GCMs described in Sect. 2.2.1 and 2.2.2 were temporally (time), spatially (latitude, longitude) and

trajectories can also travel at low altitudes. In this improved collocator, when the linear interpolation in the nearsurface trajectories would result into a missing value, nearest-neighbour interpolation is used instead. In that wayThus,
extrapolation of values can be avoided and information for trajectory points that are within the data domain retained. The
collocated GCM data from the airmassair mass trajectory arrival times, i.e., times when the air mass is located at
SMEAR II, are used to represent the conditions at SMEAR II, thus facilitating direct comparison to observational data
obtained at the site.

trajectories coordinates was used, is that the raw precipitation fields from ERA-Interim are employed in this work by collocated collocating them to the airmassair mass trajectories in a post-processing step (as for the variables extracted from GCMs described above), similar to the variables extracted from the GCMs mentioned above. This approach was chosen to retain the original numerical precision of ERA-Interim (and GCM) precipitation data, ensuring accurate alignment with co-located GCM variables (e.g., aerosol size distributions and chemical composition), which HYSPLIT does not provide. Here, "consistency" refers to numerical accuracy rather than matching data sources. This approach was selected as it allows to retain the original numerical precision from ERA-Interim (and the GCMs) precipitation data, thus ensuring consistency with the other collocated GCM variables (e.g., aerosol size distributions and chemical composition) which

A difference to Isokääntä et al. (2022) where the ERA-Interim precipitation internally processed by HYSPLIT onto

#### 2.4 Data harmonization between measurements and GCMs

cannot be provided in the output from HYSPLIT itself.

### 2.4.1 Temporal collocatco-location and data pre-processing

The data from the measurements (1-hourly averages) conducted at SMEAR II was temporally collocated with the ERA-Interim derived back-trajectory arrival times (3-hourly). Additionally, the GCM derived trajectories (3-hourly) were only collocated with the times when aerosol observations were available. By adopting this approach, only GCM trajectories corresponding to existing data points in observations were retained and utilized in further analysis, unless noted otherwise. The importance of temporal collocation for model evaluation is discussed, for example, in Schutgens et al. (2016). Harmonisation of the measured aerosol size distribution and composition with the corresponding variables available from the GCMs are described in Sect. 2.4.2 and 2.4.3.

For consistency with Isokääntä et al. (2022) identical pre-processing is applied here to the in-situ aerosol observations before the temporal eollocatco-location described above. In the pre-processing Thus, data points for which the measured wind direction was between 120 and 140 degrees were removed due to possible influence of strong VOC (volatile organic compound) emissions from the local sawmill (Heikkinen et al., 2020; Liao et al., 2011). In addition, trajectories crossing the area of Kola Peninsula were excluded as in Isokääntä et al., (2022) due to strong pollution sources within the area (Heikkinen et al., 2020; Kulmala et al., 2000; Riuttanen et al., 2013). This led to aerosol size distribution data covering the years between 2005 and 2018 (number of final data rows/trajectories: 30688) and aerosol chemical composition for the years between 2012 and 2018 (number of final data rows/trajectories: 6174). How these data points are dDistribution of the data pointsed over the years are shown in Figures S2 and S3-in-Sect. S3. The resulting final transport paths of the trajectories can be seen in Figure S4 and S5.

#### 2.4.2 Aerosol particle number size distribution

size range (d<sub>p</sub> = 3-1000 nm). For UKESM1, complete log-normal particle number size distributions (Seinfeld and Pandis, 2016) were calculated by using the modal parameters (dry diameters, number concentrations and geometric mean diameters) given by the model. The number size distribution is discretised into the same size grid as the observations i.e., the bin midpoints are identical to the ones available from the DMPS measurements. This approach was possible as in SMEAR II the size grid DMPS applies stays constant over the whole investigated period. This harmonization was conducted for each hour along the airmassair mass trajectories using the collocateo-location approach described in Sect. 2.3.2 as UKESM1 provided all needed modal parameters for calculation of the full particle number size distributions

The DMPS (differential mobility particle sizer, e.g., Aalto et al., 2001) observations include 51 size bins in the observed

370 (PNSD) along the trajectories.

361

362

376

383

384

385

386

387

388

389

390

391

392

393

394

395

396

397

398

- For ECHAM-SALSA, the number concentrations of soluble and insoluble bins (i.e., size classes) were added together for each size bin. To make the logarithmic number size distribution comparable to UKESM1 data and DMPS measurements, the values within each size bin (i) were divided by the logarithm of the maximum size d<sub>i,max</sub> minus the logarithm of the
- minimum size d<sub>i,min</sub> i.e., by log<sub>10</sub>(d<sub>i,max</sub>)-log<sub>10</sub>(d<sub>i,min</sub>) for that size bin (see Table S3). Similar to UKESM1, this was
- 375 conducted along the trajectories. For aerosols, ECHAM-SALSA bins ranging from 3.0 nm to 1700 nm in diameter are
  - studied, as by strictly limiting to sub-micron bins ( $\leq$  700 nm), the largest sub-micron particles (700 nm < d<sub>p</sub>  $\leq$  1000 nm)
- that do contribute to the total particle mass, would be lost. However, sSensitivity analysis was conducted including only
- 378 the sub-micron bins, and none of the conclusions changed.
- Integrated variables, such as total number and mass concentrations (for submicron particles) were calculated from the particle number size distributions by assuming the particles are spherical and have a constant density of  $\rho = 1.6 \text{ g cm}^3$ .
- This density corresponds to the average density of particles observed at SMEAR II (e.g., Häkkinen et al., 2012). Again,
- these quantities were calculated for each hour (i.e., 96 data points, see Sect. 2.3.1) along every single air mass trajectory.

### 2.4.3 Chemical composition

Observational data for organic aerosol (hereafter OA) and sulfate (hereafter SO<sub>4</sub>) was obtained using observations from ACSM (aerosol chemical speciation monitor, Ng et al., 2011) which is most efficient at measuring particles with ~ 75-650 nm of vacuum aerodynamic diameter, passing through particles up to 1 µm (Liu et al., 2007). For UKESM1, Aitken and accumulation mode are used in this context by summing the mass mixing ratios (MMR, kg of species per kg of air) of these modes, including both soluble and insoluble modes when available. Due to the definition of the modes in UKESM1, these correspond to particle diameters between 10-500 nm (see Sect. S1.1), thus having large overlap with the size range most efficiently represented in ACSM. The MMRs from UKESM1 and ECHAM-SALSA are converted into mass concentrations by multiplying the MMRs with the density of the air to facilitate comparisons to chemistry observations given in the units of µg m<sup>-3</sup>. Equivalent black carbon (hereafter BC) was measured with an aethalometer using a cut off diameter of 10 µm (PM<sub>10</sub>). Due to most of the absorbing particles at SMEAR II being at sub-micron range, the difference in the BC mass between PM<sub>1</sub> and PM<sub>10</sub> is only 10 % (Luoma et al., 2019). Therefore, from UKESM1, Aitken and accumulation modes are also used to estimate the total BC. In addition, to obtain SO<sub>4</sub> from H<sub>2</sub>SO<sub>4</sub> (sulfuric acid) which is the UKESM1 native output, a conversion factor is used (see Sect. S1.1). From ECHAM-SALSA, bins with diameters ranging from 19.6 nm to 700 nm (see Sect. S1.2) are used to estimate the total sub-micron OA, SO<sub>4</sub> and BC, including again both soluble and insoluble bins. Here, for ECHAM-SALSA, the largest bin of which a portion also

consists of aerosols larger than 1  $\mu$ m (700 nm <  $d_P$  < 1700 nm) is not included to ensure consistency with the ACSM measuring efficiency (which decreases from ~650 nm up to the maximum size of 1  $\mu$ m).

# ${\bf 3}\ Aerosol\ properties\ at\ SMEAR\ II-Eulerian\ comparison\ between\ observations\ and\ GCMs$

Aerosol characteristics at SMEAR II based on observations are widely reported in the literature (e.g., Dal Maso et al., 2005; Luoma et al., 2019; Heikkinen et al., 2020). For the GCMs, fewer studies looking into aerosol properties at single sites exist, but Leinonen et al. (2022), for example, conducted an extensive study comparing long term aerosol particle seasonality and trends in observations and GCMs in multiple locations, also including SMEAR II. To set the scene and provide context to GCM development since these previous studies (see also e.g., Reddington et al., 2016), a short assessment of the differences and similarities in Eulerian framework between the aerosol observations, UKESM1 and ECHAM-SALSA at SMEAR II is given here. Airmass transport between ERA-Interim and the GCMs is first assessed (Sect. 3.1), followed by the aerosol particle number size distributions (Sect. 3.2) and chemical composition (Sect. 3.1 and 3.32). This provides the necessary background information to facilitate further comparisons within the Lagrangian evaluation framework used in this work.

To ensure the differences shown in the following sections for the Eulerian analysis are not driven by diverging transport pathways between the GCMs and ERA-Interim, the airmass transport routes were inspected. The airmass transport routes in Figure S4 show very similar patterns for ERA Interim and the GCMs—as expected for simulations in which wind fields are consistently nudged to ERA-Interim reanalysis. Vertical transport differences exist (Figure S5), which can be attributed to potential temperature not being nudged, which follows standard practices (Zhang et al., 2014). For this station, however, these differences are relatively small, and the largest differences are in areas with low frequency of trajectories. Therefore, any observed differences in the analyses presented in the following sections are unlikely to be dominated by differences in the airmass transport.

## 3.1 Comparison of air mass transport between ERA-Interim and the GCMs

To ensure the differences shown in the following sections for the Eulerian analysis are not driven by diverging transport pathways between the GCMs and ERA-Interim, the airmass transport routes were inspected. The airmass transport routes in Figure 1 show very similar patterns for ERA-Interim and the GCMs, i.e., the differences are, on average, very small—as expected for simulations in which wind fields are consistently nudged to ERA-Interim reanalysis. Vertical transport differences exist (Figure S5), which can be attributed to potential temperature not being nudged, which follows standard practices (Zhang et al., 2014). For this station, however, these differences are relatively small, and the largest differences are in areas with low frequency of trajectories. Therefore, any observed differences in the analyses presented in the following sections are unlikely to be dominated by differences in the airmass transport.

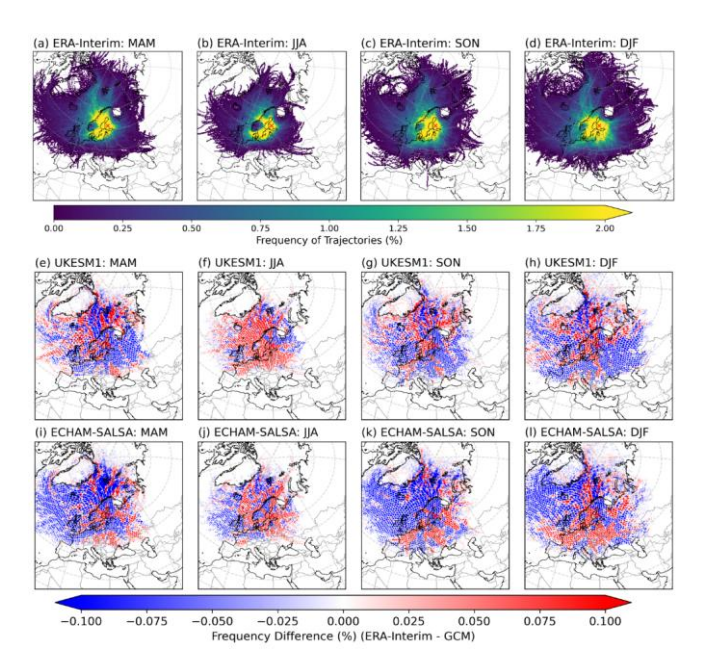


Figure 13 ERA-Interim air mass trajectory frequencies for spring (MAM), summer (JJA), autumn (SON) and winter (DJF) are shown in the top row. Frequencies for UKESM1 (e-h) and ECHAM-SALSA (i-l) are shown as differences to the ERA-Interim. Before calculating the differences, the GCM hexagonal grid (150 hexagons in the x-direction) were first regridded to match the gridding in ERA-Interim. Red cross shows the location of SMEAR II.

### 3.31 Aerosol particle number size distributions

429 |430

431

432

433

434

435

436

437

438

439

440

441

442

443

444

445

446

447

448

449

450

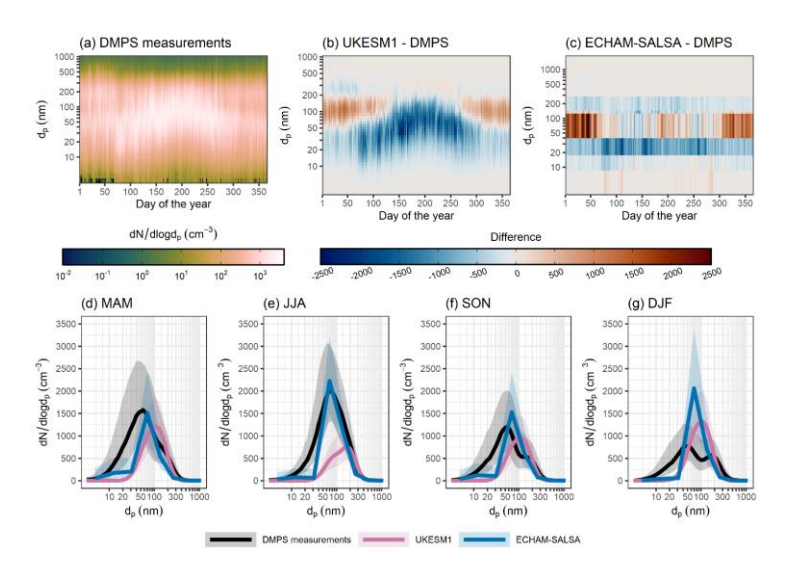
In Figure 2 particle number size distributions from the GCMs are compared with observational data at SMEAR II. The figure reveals that UKESM1 underestimates the number concentration of the small (d<sub>e</sub> < 50 nm) particles, especially during summer (Figure 2Figure 1ab-d, Table S5). This is, however, expected, as the new particle formation from boundary layer nucleation was not implemented in UKESM1 (Mulcahy et al., 2020). ECHAM-SALSA does have a better representation of the PNSD of the smaller aerosol particles during spring and summer when compared to observations (Figure 2Figure Lce), During warmer seasons, and also the absolute number concentrations agree well between observations and ECHAM-SALSA during these warmer seasons (see nucleation mode from Table S5). This, highlightsing the importance of NPF from nucleation in the boundary layer, especially in summer. During winter, however, ECHAM-SALSA does exhibit some overestimation for Aitken mode aerosols (Figure 2 Figure 1e and Aitken mode from Table S5). During winter, UKESM1 overestimates larger Aitken and accumulation mode aerosols (dp up to 200 nm) compared to the observations (Figure 2Figure 1bd and gi), but during spring the number concentration of the accumulation mode aerosols is very close to observations (367 cm<sup>-3</sup> in UKESM1 vs 352 cm<sup>-3</sup> in observations as shown in Table S5). This is somewhat surprising considering the missing growth of small particles from NPF into accumulation mode, however, this could indicate that there are from other processes that which dominate the accumulation mode. During winter (Figure 2Figure 1a and gi) the observations exhibit clear bimodal PNSD peaking around 50 and 200 nm but neither of the GCMs is able to capture this behaviour. Overall, both GCMs tend to be shifted towards the larger sizes in all seasons (Figure 2Figure 1d-gf-i), and this effect is slightly more pronounced in UKESM1\_Overall, ECHAM-SALSA-simulates better estimates of the peak values of the PNSD-overall, except in winter (Figure 1gi), when it overestimates the particle concentrations at the size range of  $d_p = 50 - 100$  nm, Median particle number size distributions (averages over the entire simulation period) for day of the year are shown in Figure 1a c followed by the differences between the DMPS measurements and the GCMs in Figure 1d e. Median (25<sup>th</sup>-75<sup>th</sup> percentiles) size distribution functions for each season are shown in Figure 1f i and the aerosol number concentrations for nucleation, Aitken and accumulation mode are shown in Table S5 for DMPS measurements and the GCMs. ECHAM-SALSA data in Figure 1c is presented in its native resolution for size bins falling between  $d_p = 3.0 - 1700$  nm and those size bins are positioned within the y-axis to the geometric mean of the ECHAM-SALSA size bins (see Table S3). To calculate the difference in Figure 1e, the measured size distribution is regridded to the ECHAM-SALSA bins by integrating between the upper and lower limit of each ECHAM-SALSA size bin.

UKESM1 underestimates the number concentration of the small (d<sub>p</sub> < 50 nm) particles, especially during summer (Figure 1a-d, Table S5). This is, however, expected, as the new particle formation from boundary layer nucleation was not implemented in UKESM1 (Muleahy et al., 2020). ECHAM-SALSA does have a better representation of the PNSD of the smaller aerosol particles during spring and summer when compared to observations (Figure 1e), and also the absolute number concentrations agree well during these warmer seasons (see nucleation mode from Table S5), highlighting the importance of NPF from nucleation in the boundary layer, especially in summer. During winter, however, ECHAM-SALSA does exhibit some overestimation for Aitken mode aerosols (Figure 1e and Aitken mode from Table S5).

During winter, UKESM1 overestimates larger Aitken and accumulation mode acrosols (d<sub>p</sub>-up to 200 nm) compared to the observations (Figure 1d and i), but during spring the number concentration of the accumulation mode acrosols is very close to observations (367 cm<sup>-3</sup> in UKESM1 vs 352 cm<sup>-3</sup> in observations as shown in Table S5). This is somewhat surprising considering the missing growth of small particles from NPF into accumulation mode, however, this could indicate from other processes which dominate the accumulation mode. During winter (Figure 1a and i) the observations exhibit clear bimodal PNSD peaking around 50 and 200 nm but neither of the GCMs is able to capture this behaviour. Overall, both GCMs tend to be shifted towards the larger sizes in all seasons (Figure 1f-i), and this effect is slightly more pronounced in UKESM1. ECHAM-SALSA simulates better estimates of the peak values of the PNSD overall, except in winter (Figure 1i), when it overestimates the particle concentrations at the size range of d<sub>p</sub> = 50 – 100 nm.

Field Code Changed

Field Code Changed



## 3.32 Chemical composition of the aerosols

478 |479

480

481

482

483

484

485

486

487

488

489

490

491

492

493

494

495

496

497

498

499

500

501

502

Particle chemical composition as a mass concentration for each chemical species from the composition measurements and the GCMs at SMEAR II (trajectory receptor location) is illustrated in Figure 3Figure 2, and the seasonal patterns are typical for this location, a d (numeric values are shown in Table S6) and the monthly variations are shown in Figure 2e g. Mass fractions are shown in Figure S6. The seasonal patterns are typical for this location, having lL argest concentration of organic material is present during summer (JJA) and smallest in winter (DJF). Both GCMs also have pronounced OA concentration during summer compared to the other seasons, and UKESM1 captures the pronounced OA concentrations observed during summer particularly well (median OA 2.0 µg m<sup>-3</sup> and 2.2 µg m<sup>-3</sup> in UKESM1 and observations, respectively, Table S6). A portion of the small underestimation of the OA concentrations of the GCMs during spring and summer could, however, be influenced by the height of the observations as chemical composition measurements are conducted at the surface whereas the GCM data shown here are at the trajectory arrival point height at the receptor station (100 m.a.g.l.). Scale difference likely also plays a role-in the differences overall, as the point measurements are compared with the GCM grid box values interpolated to airmassair mass trajectories. Monthly data (Figure 3Figure 2e) shows the second OA peak for the observations to be in February, as expected based on Heikkinen et al. (2020), and in ECHAM-SALSA this peak falls on January. UKESM1 has this peakpeaks in February, but the difference in the concentrations (compared to observations) between February and January/March is very small. The seasonality of the OA concentrations presented here for both observations and GCMs also agrees with the results from Blichner et al. (2024) who presented the same GCMs but for a different time period. Differences in the monthly peak concentration can be observed for BC too, where observations and UKESM1 peak in February, but ECHAM-SALSA exhibits the largest BC concentrations in January (Figure 3Figure 2g).

In general, even though a perfect harmonization of the particle chemical composition data between observations and GCMs is not achieved (see Sect. 2.4.3), the median concentrations between observations and GCMs agree relatively well when the overall seasonality is inspected (Figure 3Figure 2a-d); the concentrations are dominated by OA in all seasons, followed by SO<sub>4</sub> and BC. Inspection of the monthly median concentrations (Figure 3Figure 2e-g), however, revealed that differences also exist.

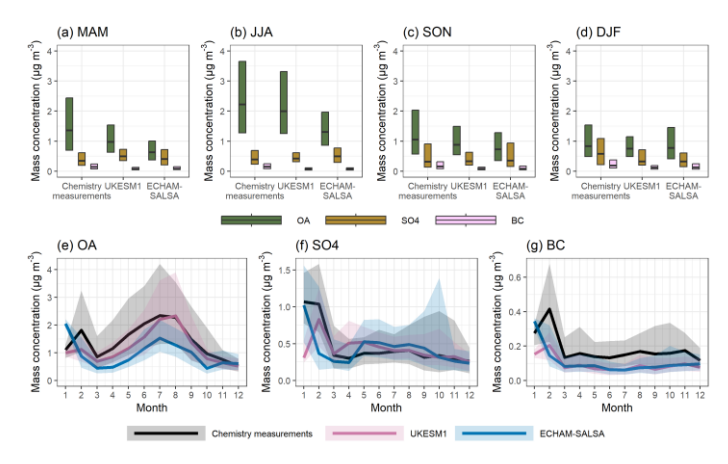


Figure 32 Average seasonal mass concentration of sub-micron OA, SO4 and BC at SMEAR II from the chemical composition measurements, UKESM1 and ECHAM-SALSA is shown in (a)-(d). Black horizontal lines show the median and the boxes extend between 25th and 75th percentiles. Monthly median (lines) concentrations and 25th-75th percentiles (shaded areas) are presented in (e)-(g). To ensure the differences shown in the following sections for the Eulerian analysis are not driven by diverging transport pathways between the GCMs and ERA-Interim, the airmass transport routes were inspected. The airmass transport routes in Figure S4 show very similar patterns for ERA-Interim and the GCMs—as expected for simulations in which wind fields are consistently nudged to ERA-Interim reanalysis. Vertical transport differences exist (Figure S5), which can be attributed to potential temperature not being nudged, which follows standard practices (Zhang et al., 2014). For this station, however, these differences are relatively small, and the largest differences are in areas with low frequency of trajectories. Therefore, any observed differences in the analyses presented in the following sections are unlikely to be dominated by differences in the airmass transport.

#### 4 Lagrangian analysis of overall effects of integral precipitation on aerosols at SMEAR II

In this section we use the Lagrangian framework to investigate the potential wet removal of the aerosols. In Sect. 4.1 we-

first examine the impact of using vertically resolved liquid precipitation (UKESM1 only), which has not previously been

done for Lagrangian trajectory analyses. Then we inspect the relationship between accumulated precipitation and aerosols

for the two GCM s used in this study: UKESM 1 and ECHAM-SALSA. In Sect. 4.2 we focus on total aerosol mass and

number, and in Sect. 4.3 we focus on the OA, BC, and SO4 portions of the total mass for submicron-size aerosols. Then,

528 in Sect. 4.4, the processes controlling the precipitation-aerosol relationships presented in the previous sections are 529

investigated, and the differences are discussed in detail between the GCMs (Sect. 4.4.1) and within each GCM (Sect.

4.4.2). Supplementary analysis assesses the representability of the models employed here amongst larger group of GCMs

531 (Sect. S4).

522

523

524

525

526

527

530

532

533

534

535

536

537

540

541

542

543

544

545

547

548

549

550

551

552

553

554

555

556

557

558

559

#### 4.1 Assessment of surface vs. vertically resolved precipitation in Lagrangian wet removal

In earlier studies assessing aerosol-precipitation relationships at SMEAR II using the Lagrangian framework (e.g., Isokääntä et al., 2022; Khadir et al., 2023; Tunved et al., 2013) the vertical position of the trajectories with respect to the

precipitating clouds was not considered. The approach, therefore, does not allow for separation between in-cloud and

below-cloud precipitation scavenging. Instead, it provides us with the overall effect of precipitation (hereafter noted as

wet removal), in which the surface precipitation is used as a proxy for the experienced precipitation by the air mass. This

538 also means that it could include trajectories that travel above the precipitation, potentially confounding interpretation of

539 the results.

> For this study, it was possible to examine the impact of this simplification was examined by extracting the vertically resolved liquid precipitation from UKESM1, which can be compared to the surface precipitation (see Appendix A). Based on this analysis, it was possible to conclude (see e.g., Figure A1) that for this station the surface precipitation is a relatively good proxy for the experienced precipitation by the air mass. Therefore, and to be able to include the effects due to snowfall, which was unfortunately not extracted with high enough vertical resolution from UKESM1, the surface precipitation is continued to be used in this study. Vertically resolved precipitation was not available from ECHAM-

546 SALSA.

Before exploring the relationships between accumulated precipitation and aerosols in UKESM1 and ECHAM-SALSA,

the representativity of UKESM1 and ECHAM SALSA compared to a larger group of GCMs from the AeroCom cohort

(simulation years 2009-2013) is assessed. Summaries of these other GCMs are given in Appendix B. For this comparison,

the particle size distribution variables and total precipitation (see Table S4) were inspected. From the aerosol variables

the full particle number size distributions were calculated in a similar manner as for UKESM1 (see Sect. 2.4.2), followed

by integration to obtain total mass and number concentrations for each model. Figure 3 shows the normalized (see first

paragraph in Sect. 4.1) particle mass and number concentrations as a function of the accumulated total precipitation

(Figure 3a b), the sample size (Figure 3c) for each precipitation bin and the mean rainfall rates along the trajectories

(Figure 3d) for each of the GCMs. For normalized aerosol mass, all the GCMs except NorESM exhibit relatively similar

behaviour up to 5 mm of accumulated precipitation. For normalized aerosol number, the differences between the models

are larger. NorESM has very strong initial decrease for both particle mass and number, which starts exhibiting increase

for both with increasing accumulated precipitation after ~5 mm of accumulated precipitation. The average rainfall rates between the GCMs (Figure 3d) are relatively close to each other. CAM5 and NorESM exhibit slightly smallest rates,

Formatted: Normal

Formatted: Subscript

whereas UKESM1 and the tree ECHAM models, ECHAM SALSA, ECHAM HAM and ECHAM HAM P3, exhibit slightly higher rates. Overall, neither UKESM1 nor ECHAM SALSA are presenting the extremes, i.e., they are relatively close to the GCM ensemble mean (not shown) when representing the aerosol accumulated precipitation relationships. Therefore, these GCMs are good examples amongst this larger group of GCMs.

In this section the investigation begins by inspecting the relationship between accumulated precipitation and aerosols for the two GCMs used in this study: UKESM1 and ECHAM-SALSA. The analysis is simplified by removing the size-dependent component noted in previous literature (see e.g., Figure 3 in Isokääntä et al., 2022 and Figure 4 in Khadir et al., 2023) by first focusing on total aerosol mass, number (Sect. 4.1) and the OA, BC, and SO<sub>4</sub> portions of the total mass (Sect. 4.2) for submicron-size aerosols. Then, in Sect. 4.3, the processes controlling the precipitation aerosol relationships presented in the previous sections are investigated, and the differences are discussed in detail between the GCMs (Sect. 4.3.1) and within each GCM (Sect. 4.3.2).

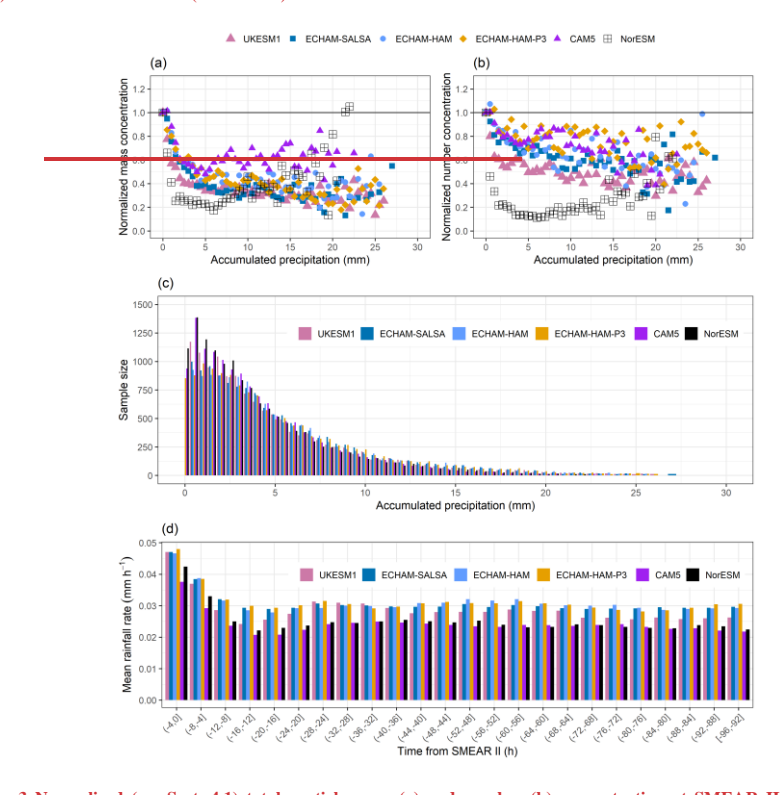


Figure 3 Normalized (see Sect. 4.1) total particle mass (a) and number (b) concentration at SMEAR II as a function of accumulated total (stratiform and convective, including both liquid rain and snow) precipitation along the 96-h long airmass trajectories for the different GCMs. The coloured points in (a) and (b) show the median values for each 0.5 mm bin of accumulated precipitation when the number of data rows in the bin was 10 or larger. The sample size for the corresponding 0.5 mm bins is shown in (c) and the average rainfall rates along the trajectories (averaged over 4-hour periods for visual clarity) are shown in (d). The shown data have been temporally harmonized within the GCMs, thus including data between 2009 and 2013.

#### 4.21 Relationship between precipitation and aerosol mass and number concentrations

The relationship between the normalized particle mass and number as a function of accumulated stratiform precipitation (including both liquid and snow) for the temporally collocated observations and UKESM1 and ECHAM SALSA are shown in Figure 4 for summer (June, July and August) and wintertime (December, January and February) data. Figure 4c displays the sample size for each corresponding 0.5 mm bin of accumulated precipitation. The relationship between the normalized mass and number concentration with the average experienced rainfall rate along the trajectory is presented in Figure S7. In the analysis presented here, the focus is on summer and winter, to see whether the observed source receptor relationship between aerosols and precipitation, a proxy for removal, is dependent on the season. Inspection of the seasonality is relevant, as differences in the relationships could be driven by different particle size distributions at the station which vary by season due to differences in meteorology (e.g., origin of air masses, temperature and sunlight) along the airmass trajectories. Seasonality also impacts to the type of the precipitation (liquid vs snow and stratiform vs convective, for example). Normalization of the median mass/number concentration to the median mass/number when accumulated stratiform precipitation is zero is employed here in attempt to minimize the effects due to the differences in the native particle number size distributions (e.g., Figure 1), which further cause differences in the total mass and number concentrations, and inspect the actual derived removal by precipitation instead. Non normalized mass and number concentrations are shown in Figures S8 and S9, and those are similar to Isokääntä et al., (2022) which employed whole year data and total precipitation.

The removal of the normalized masses (dp = 3-1000 nm, Figure 4Figure 4a) by accumulated stratiform precipitation for observations and both GCMs exhibit exponential decrease reaching asymptotic behaviour after ~10 mm of accumulated precipitation (after 5 mm for UKESM1 during summer). Normalization of the median mass/number concentration to the median mass/number-median value under zerowhen accumulated stratiform precipitation is used in this study. zero is employed here in attempt This approach aims to minimize the effects due to the influence of differences in the native particle number size distributions (e.g., Figure 1), which affect further cause differences in the total mass and number concentrations, and inspect the actual derived removal by precipitation instead instead highlight the removal attributable to precipitation.

For the particle number concentration (dp = 3-1000 nm), on the other hand, there are clear differences, which also depend on the seasonthere are clear seasonal differences (Figure 4b). ECHAM-SALSA and the observations show clear seasonal differences in particle number removal, with much more efficient removal in winter than in summer. UKESM1, however, does not display this seasonal contrast—likely because it lacks boundary layer nucleation, a key source of small particles during summer, which leads to similar particle number concentrations across seasons. Here ECHAM-SALSA and the observations show distinctly different removals between the two seasons, with wintertime removal being much more efficient than summertime. UKESM1, on the other hand, does not exhibit such large seasonal difference in the removal of the particle number, likely due to the buffering effect due to missing particle source (NPF) in the boundary layer. Inspection of the seasonality is relevant, as differences in the relationships could be driven by different particle size distributions at the station which vary by season due to differences in meteorology (e.g., origin of air-masses, temperature and sunlight) along the air mass trajectories. Seasonality also impacts to the type of the precipitation (liquid vs snow and stratiform vs convective, for example).

<u>Figure 4</u>Figure 4c shows that the seasonal patterns (e.g., more samples for smaller precipitation values in summer) in the distribution of accumulated precipitation are similar for both models and observations, thus unlikely driving differences

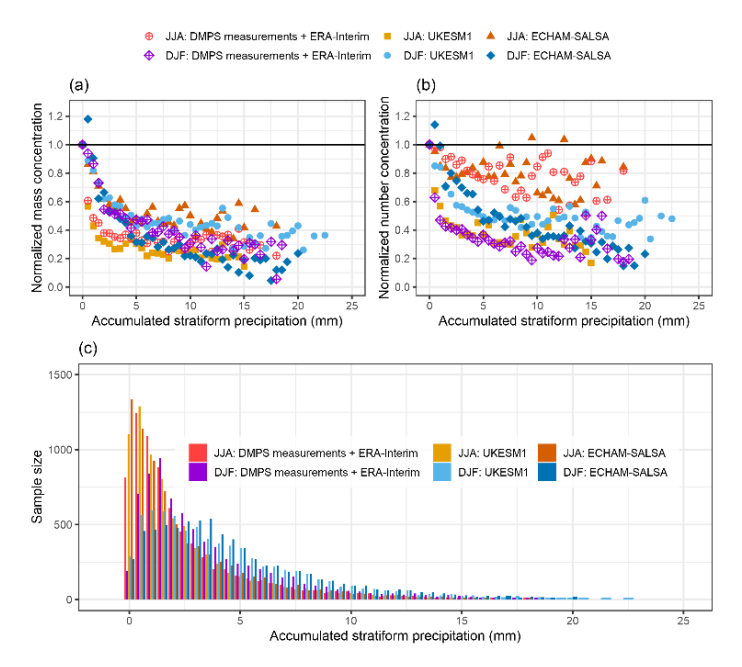


Figure 44 Normalized total ( $d_p = 3-1000$  nm) particle mass (a) and number (b) at SMEAR II for summer (June, July and AugustJJA) and wintertime (December, January and February DJF) as a function of accumulated stratiform surface precipitation (incl. both liquid and snow) along the 96 hour long airmassair mass trajectories for observations (DMPS measurements paired with ERA-Interim trajectories) and GCMs. The coloured points show the median values for each 0.5 mm bin of accumulated precipitation when the number of data rowstrajectories in the bin was 10 or larger. The sample size for each corresponding bin is shown in (c).

## 4.32 Relationship between precipitation and aerosol chemical composition

The normalized masses of OA, BC, and SO<sub>4</sub> in submicron-sized particles as a function of accumulated stratiform precipitation (including both liquid and snow) for the observations and the GCMs is shown in <u>Figure 5</u> (see also Figure S<sub>2</sub>10 showing the same data but grouped differently for easier comparison between the species). The division into warmer and colder months follows the monthly median temperatures (measured at the site) as in Isokääntä et al. (2022). This division is used instead of the stricter summer/winter division used in Sect. 4.1, as the chemical composition observations are more limited (see Figure S<sub>3</sub>) and thus stricter division by season would reduce the statistics too much

for reliable analysis. The sample sizes for each precipitation bin are presented in Figure 5g-h, and during warmer months, they agree well during warmer months between the GCMs. During colder months (Figure 5Figure 5h) more differences emerge for the smaller precipitation bins (< 3 mm of accumulated precipitation).

The general patterns between the observations and GCMs are similar for all species—exponential decrease is observed for the mass concentrations, similar to the relationships between total particle mass and precipitation shown in Figure 4Figure 4a. The seasonal differences for the total particle mass (Figure 4Figure 4a) and the chemical constituents are comparable despite the different approach used to separate the data into temperature regimes instead of seasons. During the colder months (Figure 5Figure 5d-f), ECHAM-SALSA exhibits the most efficient removalreduction for all the three species, as expected based on the removalreduction of the total aerosol mass (Figure 4Figure 4a). During the warmer months (Figure 5Figure 5-c), UKESM1 tends to show more efficient removalreduction than ECHAM-SALSA, the effect being most pronounced for OA. This is in line with the derived removalreduction of total particle mass and number during summer shown in Sect. 4.1 (Figure 4Figure 4a-b), in which ECHAM-SALSA exhibited stronger removalreduction during winter and UKESM1 during the summer.

The observational data presented by Isokääntä et al. (2022) showed that the removalreduction of SO<sub>4</sub> due to accumulated total precipitation in the warmer months was less efficient compared to other species, despite SO<sub>4</sub> being highly hygroscopic and thus relatively easily activated as a cloud droplet. This is relevant also in this study, as the activation into cloud droplets followed by precipitation is the dominant removalreduction mechanisms also for the mass of the different chemical species (discussed in more detail in Sect. 4.43). Similar to Isokääntä et al. (2022), the derived removalreduction for SO<sub>4</sub> is less efficient (i.e., smaller end concentrations are reached) compared to OA and BC also here for the observations and UKESM1 (Figure S940a-b), though the differences between species are overall smaller but still statistically significant (Kruskal-Wallis rank sum test, p < 0.001). For ECHAM-SALSA, the derived removals between OA and SO<sub>4</sub> do not differ (Figure S940c, Kruskal-Wallis rank sum test, p = 0.2) during warmer months, but BC shows more efficient removalreduction with the accumulated stratiform precipitation than OA and SO<sub>4</sub>. This could be arising from the fact that, in ECHAM-SALSA, all BC is basically in the soluble particles (Figure S104b) but OA and SO<sub>4</sub> can reside in the insoluble particles as well.

Isokääntä et al. (2022) hypothesized that the low derived removal efficiency of SO<sub>4</sub> during warmer months could be caused by the species being distributed to different sizes depending on the season. Inspection of the size resolved chemical composition from the GCMs (Figure S104), however, is not able to fully explain the observed seasonal differences: SO<sub>4</sub> in the GCMs is almost completely distributed to the soluble accumulation mode, and the seasonal differences are only minor. In ECHAM-SALSA, small contribution of insoluble SO<sub>4</sub> in the accumulation mode is present, but the difference between the seasons is small (Figure S104b). Other possible explanations could include, for example (but not limited to), mixing state (internal/external) of the particles and production of SO<sub>4</sub> through cloud processing, which could compensate for the removal reduction by stratiform precipitation.

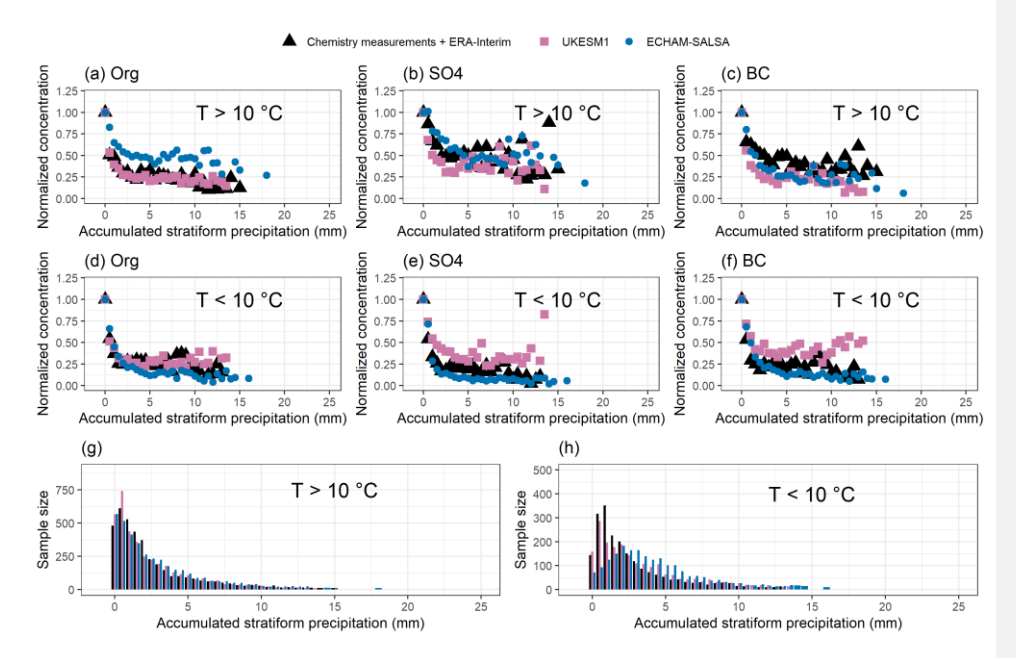


Figure  $\frac{55}{2}$  Normalized mass concentration for submicron OA, SO<sub>4</sub> and BC at SMEAR II as a function of accumulated stratiform surface precipitation along the 96 hour long airmassair mass trajectories for observations (chemistry measurements paired with ERA-Interim trajectories) and the GCMs for warm (T > 10 °C, (a)-(c)) and cold (T < 10 °C, (d)-(f)) months. The coloured points show the normalized median values for each 0.5 mm bin of accumulated precipitation when the number of data rowstrajectories for the bin was 10 or larger. The sample size for each corresponding 0.5 mm bin is shown in (g)-(h).

## 4.43 Process-chain evaluation for understanding the relationship between precipitation and aerosols

To understand which processes are driving theunderstand the differences between GCMs and observations in Figure 4Figure 4 and Figure 5Figure 5, investigation of the relative importance of different pathways among wet removal is neededwe assess the relative importance of wet removal pathways. As already discussed in previous literaturePrior studies (Isokääntä et al., 2022; Tunved et al., 2013; Wang et al., 2021), it is likelysuggests that in-cloud scavenging particle activation followed by rainout, (particles nucleating into cloud droplets) followed by removal due to rainout is, on average, is the dominantting removal mechanism in the studied environment for submicron-sized particles in this region. For UKESM1 the relative contributions of the different removal types were additionally inspected, as those were available from the model output. These relative contributions were derived from the median scavenging coefficients for each removal types (below-cloud impaction, nucleation followed by rainout, and plume scavenging, see Sect. S2) were quantified using median scavenging coefficients provided along the trajectories (see Sect. S2). These scavenging coefficients represent the removal within the total atmospheric column, median values along complete trajectories being 0.040 (JJA) and 0.028 (DJF) moles s<sup>-1</sup> for impaction, 0.700 (JJA) and 0.191 (DJF) moles s<sup>-1</sup> for nucleation followed by rainout and 0.001 (JJA) and 0.000 (DJF) moles s<sup>-1</sup> for plume scavenging.

Indeed, as demonstrated As shown in Figure 6 Figure 6 for organic aerosol (OA), (which dominates the particle mass in SMEAR II, e.g., Heikkinen et al., (2020), scavenging through nucleation (i.e., aerosol activation to cloud droplets

Formatted: Superscript
Formatted: Superscript

Formatted: Superscript

|702

followed by precipitation) on average dominates removal during transport along the trajectories. nucleation followed by rainout dominates removal. Relative contributions of the different removal processes for other chemical species, Similar patterns are seen for SO<sub>4</sub> (H<sub>2</sub>SO<sub>4</sub>) and BC (, are shown in Figure S112), and those also imply removal through nucleation is the dominating process within supporting that in-cloud removal is the main process in this region. Therefore, in agreement also with, consistent with the findings of Isokääntä et al. (2022), in UKESM1 it is likely that particles nucleating into cloud droplets followed by rainout dominates the removal of sub-micron sized particles within our study area.

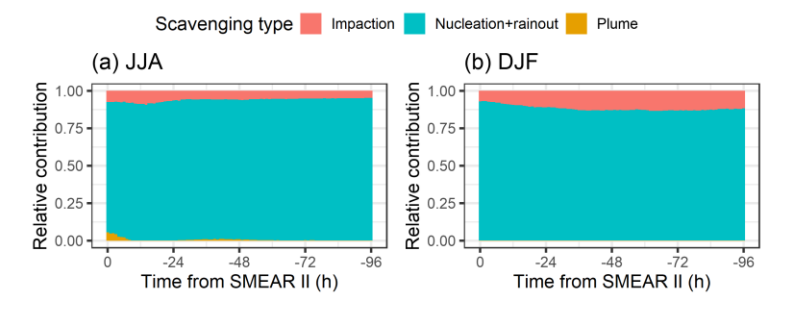


Figure 66 Relative contributions of the different removal pathways in UKESM1 for OA in (a) summer/JJA and (b) winter as a function of time from SMEAR II. Impaction refers to the below-cloud impaction scavenging, nucleation + rainout describes the activation process followed by removal of the particles via the formed raindrops, and plume scavenging is the removal due to convective clouds.

As noted in the paragraph-above, nucleation followed by removal of the particles by precipitation is driving the observed relationships shownprecipitation-driven removal explains the patterns in Figure 4Figure 4 and 45. To understand differences in this process across models, we compare key variables along air mass trajectories related to in-cloud removal. Hence, comparison of key variables along the airmass trajectories for the GCMs is provided to probe the differences in the actual process chain related to in cloud removal. The importance of the associated sub-grid scale processes, and variables underpinning droplet activation, have also been highlighted in pPrevious studies (Dusek et al., 2006; Ohata et al., 2016; Partridge et al., 2012; Reutter et al., 2009): have emphasized the role of sub-grid processes and variables influencing droplet activation, such as particle size and vertical air motion. We therefore examine how model representations of activation—affected by sub-grid vertical velocities and aerosol size distributions—influence removal. Therefore, these variables are also addressed here by inspecting how differences in the representation of activation (controlled e.g., by sub-grid scale vertical movement of air) affect removal via nucleation, and also exploring, for example, the precipitation intensity during the travel of the air mass.

Key variables controlling the aerosol activation into cloud droplets (presented in Figure 7-Figure 7a-j) include shows the number of particles having with diameter  $d_p > 80$  nm ( $N_{80}$ ) and sub-grid scale vertical velocities (referred as updraughtsupdraught velocities from hereon for conciseness), which control droplet formation. The aAccumulation mode particles (i.e.,  $N_{80}$ ) are of special interest, as these sizes are mostare likely to activate to cloud droplets (Croft et al., 2010; Partridge et al., 2012), and updraught velocities drive supersaturation needed for activation, within the sub-micron size range, thus being descriptive of the available cloud condensation nuclei (CCN). The updraught velocities, on the other hand, control the vertical air movement: ascending air cools adiabatically increasing the water saturation to

 $\frac{\text{supersaturation needed for condensation. The resulting fraction of activated particles}{\text{activated fraction}} \underbrace{(N_{\text{gct}}/N_{\text{Jot}})}_{\text{is shown}}$ in Figure 7Figure 7k-o, and the rainfall rates (at the surface) are presented in Figure S123. In addition, total number of particles ( $N_{tot}$ ) and total mass of the particles ( $M_{tot}$ ) at the submicron range, accompanied with the airmassair mass heights and number of activated particles (Nact) along the trajectories are presented in Figure S134. Chemical composition, relevant for hygroscopicity and droplet formation, is shown in Figure S15.In addition to particle size, also chemistry has an impact on the droplet formation potential via hygroscopicity, hence the particle chemistry along the trajectories is also inspected (Figure S15). Together, these parameters control the cloud droplet formation, and their relationships determine factors determine whether the regime is the aerosol- or updraught limited (Reutter et al., 2009). Figure 4 and Figure 5 showed strong seasonal contrasts, and seasonal differences in N80, updraughts, and activation are also evident during transportexhibited strong seasonal differences between GCMs and seasonal differences in the key variables (N<sub>80</sub>, updraughts and activated fractions) can also be observed during the airmass transport (Figure 7Figure 7). Section 4.3.1 discusses seasonal characteristics within each GCM, followed by a model–observation comparison in Sect. 4.3.2.To further understand the role of activation on these differences, the seasonal characteristics within each of the GCMs are explored first (Sect. 4.3.1), before discussing the differences between the GCMs and observations (Sect. 4.3.2).

725

726

727

728

729

730

731

732

733

734

735

736

737

738

739

740

741

Formatted: Subscript

Formatted: Subscript

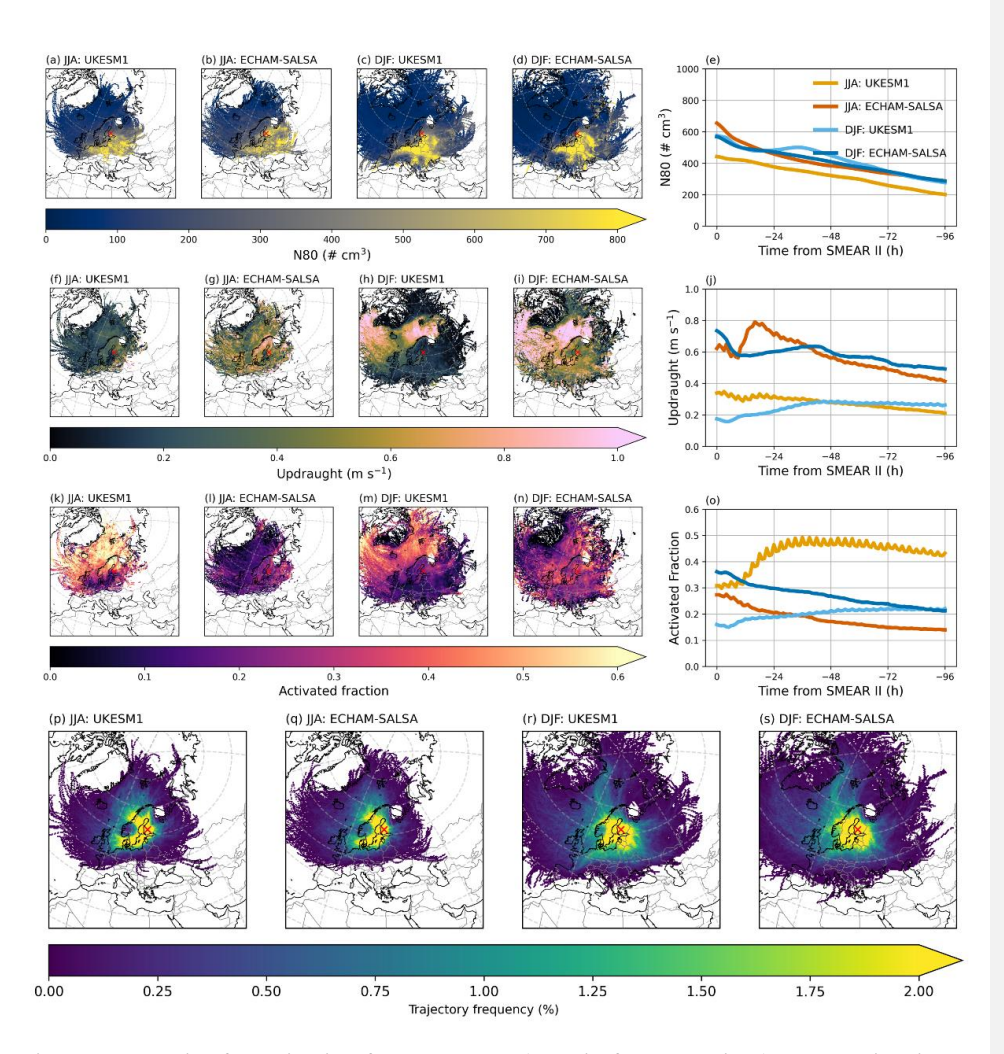


Figure  $\frac{73}{1}$  The evolution of the main drivers for the wet removal (nucleation followed by rainout) along the trajectories. The first row from the top displays the  $N_{80}$  (number of particles for which  $d_p > 80$  nm), the second row shows the sub-grid scale updraughtsupdraught velocities (m s<sup>-1</sup>), third row displays the activated fraction of particles, and the bottom row shows the corresponding trajectory frequencies. For the maps, means are calculated for each hexagonal gridbox (grid resolution being 150 in the x-direction) that the trajectory crosses, and for the rightmost panels, means have been calculated for each hour along the trajectory. For the updraughtsupdraught velocities and activated fractions, only values when trajectory is in-cloud are shown.

# 4.43.1 Seasonal differences within each GCM

In UKESM1, the derived removal for the particle mass during summer is clearly stronger, especially up to  $\sim$ 10 mm of accumulated precipitation, compared to winter (Figure 4Figure 4a). For the particle number, the differences between

Formatted: Font: Not Bold

summer and winter are less pronounced, and similar concentrations at the receptor station are reached (Figure 4Figure 4b) with high accumulated precipitation. A seasonal difference in the absolute values of N<sub>80</sub> can be observed, the number concentration being approximately 100 #particles cm<sup>-3</sup> larger during winter compared to summer (Figure 7Figure 7e). This difference, wintertime values being larger, is also seen in N<sub>tot</sub> (Figure S134e). As stated in Sect. 2.2.1, the boundary layer nucleation is absent in UKESM1—a process being especially frequent around SMEAR II during spring and summer (Nieminen et al., 2014). This is likely the cause for the observed differences in N<sub>tot</sub> as the model lacks large portion of the smaller particles during summer. For the mass, however, the summertime M<sub>tot</sub> is larger (Figure S14jS13j). This could imply that UKESM1 has more numerous medium-sized particles during summer, or, that on average, the particles in summer are larger compared to winter, thus having larger contribution to particle mass. Figure 2Figure 1 supports the latter scenario, showing the average PNSD at SMEAR II peaking at larger particle sizes in summer compared (~200 nm, Figure 2Figure 1g) to winter (~100 nm, Figure 2Figure 1i).

The seasonal differences between the updraughtsupdraught velocities in UKESM1 are small, until about 48 hours before arrival (Figure 7Figure 7j). After that, the summertime updraughtsupdraught velocities exhibit little to no change, but wintertime updraughtsupdraught velocities decrease as the airmassair mass travels closer to SMEAR II. These differences relatively close to the receptor station can be attributed to the geographical distribution of the updraughtsupdraught velocities: close to SMEAR II (across Finland, Sweden and Norway, for example), the values are larger in summertime (Figure 7Figure 7f) compared to wintertime (Figure 7Figure 7h). These regions coincide with areas of the high trajectory frequency, meaning most air masses pass through them. As a result, the elevated updraught velocities in these regions strongly influence the averages shown in Figure 7j. ies; thus, the high updraughts are being reflected on the averages irrespective of transport direction in Figure 7j.

compared to about one fifth in winter. These seasonal differences align with the spatial patterns of activated fractions and trajectory frequencies (Figure 7k, p), showing particularly high values over northern Norway and extending into the Arctic Ocean. The difference in the activated fractions between summer and winter is substantial (Figure 7o), and during summer, nearly half of the acrosols activate (compared to approximately one fifth during winter). These differences along the trajectories align with the geographical distribution of the activated fractions and trajectory frequencies during summer (Figure 7k and p), where the north of Norway, for example, displays very high activated fractions. During winter, the activated fractions in this area are much lower (Figure 7Figure 7m). The  $N_{act}$ , on the other hand, displays minor differences between the seasons in UKESM1 but is slightly larger in winter. However, considering the fact that  $N_{tot}$  in UKESM1 is much higher in winter (Figure S1 $\frac{3}{4}$ e) as mentioned earlier, the larger activated fraction (derived as  $N_{act}/N_{tot}$ ) in summer

Activated fractions differ markedly between seasons (Figure 7o), with nearly half of aerosols activating in summer

The chemical composition of particles during their travel in UKESM1 (Figure S145a) reveals that overall, during summer, the mass concentration is completely dominated by soluble modes, whereas in winter, a portion of insoluble OA in the Aitken mode is also present. Soluble SO<sub>4</sub> in the accumulation mode contributes more in winter, but this is greatly compensated by soluble OA in both Aitken and accumulation modes during summer. If the higher solubility of OA in summer compensates for the lower SO<sub>4</sub> levels, this could further enhance the particle activation potential in UKESM1 during summer compared to winter. Assuming the solubility of OA compensates for the missing portion of SO<sub>4</sub> in summer, these differences could increase the particle activation potential even further during summer in UKESM1 (compared to winter).

Figure 8 shows the relationship between mean activated fraction and mean updraught velocity that the air mass experienced before arriving at SM-EAR II for the summer and winter. Another way to inspect the relationships between activated fractions and updraughts is to inspect the averages of these variables that the airmass has experienced during the travel to SMEAR II. Figure 8 displays these variables for both summer and winter. For UKESM1, the relationship between these two variables is clearly stronger in summer (slope of 2.12, Figure 8Figure 8a) compared to winter (slope 0.62, Figure 8Figure 8b). Therefore, during summer, even a very small increase in updraught could cause a very large increase in the activated fraction. Due to this, the slightly higher updraughtsupdraught velocities during summer, when the airmassair masses approach SMEAR II (Figure 7Figure 7j), could play a major role, eventually also leading to the larger activated fractions during summer. This, together with the points discussed above (such as the availability of CCN, Ntot and particle chemistry along the trajectories), likely causes the seasonal differences observed in the removal reduction of particle mass in Figure 4Figure 4a. When also considering the missing boundary layer nucleation in UKESM1 as mentioned earlier, lack of seasonality in the derived removal of total particle number in UKESM1 (Figure 4Figure 4b) can also be explained.

ECHAM-SALSA exhibits stronger removalreduction (i.e., lowersmaller concentrations are reached with increasing accumulated precipitation) during winter than in summer for both particle mass (Figure 4Figure 4a) and number (Figure 4Figure 4b). The number of particles for which 80 nm  $< d_p \le 1000$  nm (N<sub>80</sub>) is relatively similar between summer and winter, exhibiting increase from ~300 # cm<sup>-3</sup> up to ~650 #particles cm<sup>-3</sup> as the airmassair mass reaches SMEAR II. During summer, the N<sub>tot</sub> in ECHAM-SALSA is clearly larger compared to winter (Figure S134e), which is to be This is expected due to the strong contribution of small aerosols during summer (e.g., Figure 2Figure 1c). The total mass (M<sub>tot</sub>), however, is relatively alike between the seasons (FigureS134j), which is reasonable due to the similar contribution of N<sub>80</sub> in both seasons, as these particles mostly contribute to particle mass.

The updraughtsupdraught velocities in ECHAM-SALSA exhibit large location-dependent seasonal differences (Figure

TFigure 7g versus i), especially over the oceans, where the updraughtsupdraught velocities are larger during winter (Figure 7Figure 7g). However, overall, the average experienced updraughtsupdraught velocities during the transport are rather similar in magnitude between the two seasons (Figure 7Figure 7g). This overall similarity occurs because the frequency of trajectories passing over the oceans is quite low (Figure 7Figure 7s) and they therefore do not contribute to the average over all transport directions much. On average, the updraughtsupdraught velocities increase from ~0.4 m s<sup>-1</sup> up to ~0.7 m s<sup>-1</sup> as the air masses approach SMEAR II. Slightly before arrival to SMEAR II (12-36 hours before arrival), difference can be observed in the updraught behaviour: winter updraught starts decreasing around 36 hours before arrival before increasing again at the 12-hour mark. During summer, the updraught increases all the way up ~18 hours, after which its steeply decreases and increases again at the same 12-hour mark as the wintertime updraught. As these differences are taking place relatively close to SMEAR II, it is likely that they are driven by the seasonal differences in the transport and local conditions very close to SMEAR II.

Activated fractions in ECHAM-SALSA display similar trends along their transport, increasing towards SMEAR II, but the seasonal difference in the magnitude is approximately 0.1, wintertime values being larger (Figure 7Figure 7o). This difference stays nearly constant along the transport. Again, clear seasonal differences within the trajectory transport areas (Figure 7Figure 71 and n) can be observed, and as the high activated fractions during winter (Figure 7Figure 7n) do occur in high trajectory frequency areas (Figure 7Figure 7s), they are more clearly reflected in the values when averaged over all transport directions (Figure 7Figure 7o). As the seasonal differences N<sub>80</sub> in ECHAM-SALSA are negligible, it is

unlikely that the number of potential CCN is driving the seasonal differences in activated fractions and in the aerosol mass-precipitation relationships in Figure 4Figure 4a. When the  $N_{act}$  is inspected (Figure S1 $\frac{3}{4}$ t), however, somewhat larger number of particles have activated in winter compared to summer. Thus, when considering the large difference in the total number of particles (Figure S134e), the displayed differences in the activated fractions ( $=N_{act}/N_{tot}$ ) are reasonable. In addition to size, the chemical composition of the potential CCN also has an impact to their activation. Thus, we inspected the The composition of both Aitken and accumulation mode aerosols in ECHAM-SALSA, shown in Figure \$15b, along the trajectories. Comparison of the seasons in ECHAM SALSA (Figure \$145b) does reveal, however, that the particles have relatively similar soluble accumulation mode SO<sub>4</sub> contribution, for example, in both seasons. The contribution of soluble OA in the accumulation mode is slightly larger in summer, but during winter, the smaller contribution from OA (in accumulation mode) seems to be compensated by larger contribution from soluble BC in the accumulation mode. Thus, the contribution from soluble modes altogether is relatively similar between the seasons and unlikely causes large differences in the particle hygroscopicity which could impact activation. In order to investigate whether the seasonal differences in the activated fractions could also be due to slight differences in the sensitivity of activation to updraughtsupdraught velocities, we inspected the relationships between activated fractions and updraughtsupdraught velocities similar to UKESM1. For ECHAM-SALSA, the slope for summer is smaller (slope of 0.18, Figure 8Figure 8c) compared to winter (slope 0.36, Figure 8Figure 8b). Thus, during winter, when the updraught increases, the activated fraction can increase two times as much compared to summer. Therefore, despite the similar number of potential CCN in both seasons (N<sub>80</sub>, Figure 7Figure 7e), larger portion of those activate during winter, resulting to larger  $N_{act}$  (Figure S134t) and activated fractions (Figure 7Figure 7o). All these findings discussed above are consistent with the stronger removalreduction for particle mass observed for ECHAM-SALSA in winter (compared to summer) in Figure 4Figure 4a. During summer, very little to no removal reduction is observed for the particle number for ECHAM-SALSA in Figure 4Figure 4b. The particle number concentration, however, is dominated by the small aerosols

which are unlikely to activate (see also Figure \$134e and Figure 2Figure 1c). Therefore, even with high accumulated

precipitation, no clear removal reduction is observed in Figure 4Figure 4b during summer.

831

832

833

834

835

836

837

838

839

840

841

842

843

844

845

846

847

848

849

850

851

852

853

854

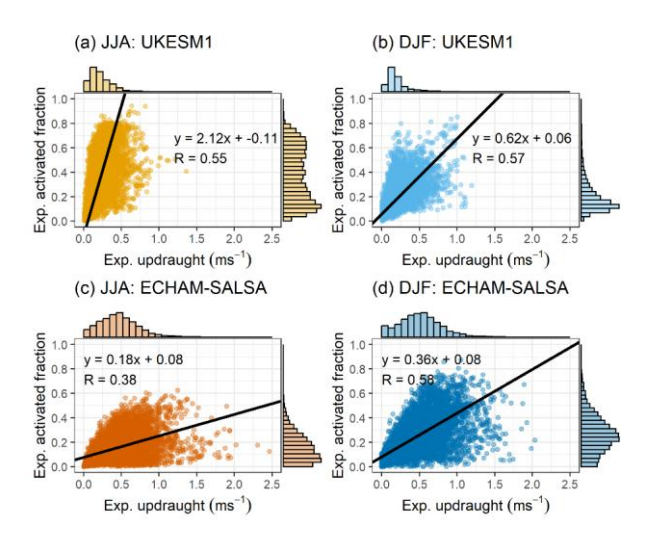


Figure 88 Average experienced activated fraction as a function of average experienced updraught velocity along the trajectories. Distribution of the values are shown with the histograms. JJA denotes summer (June-July-August) and DJF winter (December-January-February). Each coloured point denotes a median value determined from a single trajectory. The black lines show the regression line from orthogonal regression applied to the data shown and the legend show the slope, intercept and Pearson correlation (R) between the fit and the data. Note that the black regression lines extend over the whole plot area only due to visualization purposes.

## 4.43.2 Differences between GCMs and observations

Comparing the two GCMs in Figure 4 Figure 4 it is obvious that the seasonality in the aerosol-precipitation relationships is reversed: UKESM1 exhibits stronger removalreduction during summer but ECHAM-SALSA in winter. This is unlikely arising from the differences between the intensity of the precipitation during the travel of the air masses, as those are very similar between the GCMs (Figure S123a-e) within each season.

During summer, UKESM1 has less potential CCN (N<sub>80</sub>, see Figure 7Figure 7e) compared to ECHAM-SALSA, and also the updraughtsupdraught velocities are smaller in UKESM during summer, eventually leading to smaller number of cloud droplets too (N<sub>act</sub>, Figure S134t). Comparison of the contribution of different chemical species in the accumulation (as these sizes have larger contribution to the particle mass) mode (Figure S145, top row), however, reveals that UKESM1 has much larger contribution of the soluble particles. This indicates, that during summer, the particles in UKESM1 have larger hygroscopicity, and could potentially activate more easily compared to ECHAM-SALSA. However, as the resulting N<sub>act</sub> (Figure S134t) in UKESM1 is smaller than in ECHAM-SALSA, the potentially larger hygroscopicity in UKESM1 particles do not seem to have significant impact on the droplet formation. When we consider the changes in the PNSD, however, where UKESM1 has significantly less particles but with larger average size compared to ECHAM-SALSA (which has more particles but smaller average size) as shown in Figure 2Figure 1g and Figure S134e, it is sensible that larger activated fractions are observed for UKESM1 during summer as shown in Figure 7Figure 7o. The difference in the activated fraction between the GCMs, however, is somewhat larger than what could be expected based on the differences in N<sub>tot</sub> and N<sub>act</sub> alone. Thus, also the relationships between updraughtsupdraught velocities and activated fractions were inspected to gain further insight. This reveals (Figure 8Figure 8a and c), that indeed during summer, the slope between

activated fractions and updraughtsupdraught velocities in UKESM1 is significantly larger (slope 2.12, Figure 8Figure 8a) compared to ECHAM-SALSA (slope 0.18, Figure 8Figure 8c)—difference being over 10-fold. This implies that even a small perturbation in updraught velocity in UKESM1 could increase the activated fraction drastically, resulting in the very high activated fractions observed in Figure 7Figure 7o, despite UKESM1 having smaller updraughtsupdraught velocities in general. This could indicate a shift in UKESM1 cloud droplet formation from the updraught-limited regime to the transitional regime (e.g., Reutter et al., 2009). These findings align with the stronger removal reduction of particle mass in UKESM1 as shown in Figure 4Figure 4a. The removal reduction of the observed particle mass in summer lies inbetween of the two GCMs, initial removal reduction (up to 5 mm of accumulated precipitation) being more accurately represented by UKESM1.

The differences in the summertime removalreduction of particle number (Figure 4Figure 4b) likely arise from the lack of boundary layer nucleation in UKESM1, thus affecting the number concentration of the smallest aerosol particles (see e.g., Figure 2Figure 1g). As already discussed in Sect. 4.43.1, in SMEAR II, NPF is an important source of aerosols and the frequency of the NPF events has significant seasonal variation (Nieminen et al., 2014), summer and spring being most pronounced. Thus, the removalreduction of particle number in UKESM1 during summer (Figure 4Figure 4b) is similar to the removalreduction of particle mass (Figure 4Figure 4a), as both are dominated by relatively large aerosols. The summertime removalreduction of particle number in ECHAM-SALSA coincides with observations, which is to be expected as the Aitken and nucleation mode aerosol concentrations in ECHAM-SALSA are much closer to observed data than UKESM1 (Figure 2Figure 1g and Table S5).

During winter, ECHAM-SALSA exhibits stronger removal reduction of particle mass compared to UKESM1 after ~5 mm of accumulated precipitation (Figure 4Figure 4a). The N<sub>80</sub> (Figure 7Figure 7a-e) is relatively similar between the GCMs, but updraughtsupdraught velocities (Figure 7Figure 7j) have large difference: UKESM1 updraughtsupdraught velocities are below and aboverange 0.2-0.4 m s<sup>-1</sup>, whereas ECHAM-SALSA has values ranging approximately between 0.5-0.7 m s<sup>-1</sup>. The higher updraughtsupdraught velocities in ECHAM-SALSA likely lead to the larger N<sub>act</sub> (Figure S14t), thus eventually leading to the larger activated fractions for ECHAM-SALSA along most of the transport (Figure 7Figure 7o) due to N<sub>tot</sub> being relatively similar between the GCMs (Figure S134e) during winter. It should be noted, that the difference in activated fractions (Figure 7Figure 7o) far away from SMEAR II is negligible. However, this difference drastically increases when airmassair masses travel to SMEAR II: activated fraction in ECHAM-SALSA continues to increase while UKESM1 fractions stay nearly constant. Thus, it is unlikely that the similar activated fractions far away from SMEAR II significantly impact the removal reduction observed in Figure 4Figure 4a.

Comparison of the particle chemistry in the accumulation mode in winter reveals that the GCMs have (Figure S145, bottom row) relatively similar fractions of soluble material. UKESM1 tends to have more SO4, but ECHAM-SALSA more soluble OA and BC. In ECHAM-SALSA, however, the insoluble modes are not strictly insoluble but rather less insoluble compared to soluble modes (Sect. S2.3) and can thus also activate. This could lead to larger Nact (Figure S1340) and thus larger activated fraction (Figure 7Figure 70), considering that the difference in Ntot (Figure S134e) between the GCMs is clearly smaller in winter than what it was in summer. The differences in the relationships between activated fractions and updraughtsupdraught velocities for the GCMs (Figure 8Figure 8) are more subtle in winter (UKESM1 slope 0.62, ECHAM-SALSA slope 0.36) compared to the values in summertime discussed earlier. Activated fraction in UKESM1 does exhibit higher "sensitivity" for updraughtsupdraught velocities, however, due to the much larger updraughtsupdraught velocities in ECHAM-SALSA, this is likely not enough to increase the activated fraction to the

Formatted: Font: Not Bold

same level, thus leading to less efficient removalreduction. These assessments align with the particle mass removalreductions in winter shown in Figure 4Figure 4a, where particles at ECHAM-SALSA reach slightly lower end concentrations with high accumulated precipitation compared to UKESM1.

The differences in the wintertime removalreduction of particle number (Figure 4Figure 4b) are less pronounced compared to those in particle mass (Figure 4Figure 4a). Initial removalreduction seems to be more effective on UKESM1, however, after ~5 mm of accumulated precipitation, removalthe reduction in ECHAM-SALSA tends to decrease slightly morbecomes strongere. These differences between the GCMs, however, were not statistically significant (Kruskal-Wallis rank sum test,  $p \ge 0.01$ ). The observational data exhibits stronger removalreduction than the GCMs during winter for the particle number (Figure 4Figure 4b) up to ~10 mm of accumulated precipitation. After that, the observations overlap with ECHAM-SALSA. These inconsistencies could also arise from the fact that both GCMs have difficulties representing the bimodal particle number size distribution correctly during the winter months (Figure 2Figure 1i).

#### 4.4.3 Other Additional reasons for inter-model differences

920

921

922

923

924

925

926

927

928

929

930

931

932

933

934

935

936

937

938

939

940

941

942

943

944

945

946

947

948

949

950

951

952

Aside from differences driven by aerosol activation, it is important to note that during both summer and winter, additional factors can also contribute to the observed differences in the removalreductions (Figure 4Figure 4). For example, the differences in the removal reduction of the particle mass (Figure 4Figure 4b) could be influenced by the plume scavenging scheme, a feature only present in UKESM1 (see Sect. S2.4). In this process, aerosol activate into cloud droplets within the convective updraught and fall out via the main precipitation shaft of the cumulonimbus (Kipling et al., 2013; Mulcahy et al., 2020). Note that even though the particle mass is shown as a function of accumulated stratiform precipitation (Figure 4Figure 4), the airmassair mass trajectories have experienced convective precipitation too. Thus, removal via nucleation (which is more efficient for larger particles) followed by rainout in the convective plume, could also contribute. Inspection of the contribution of the precipitation types reveals that the contribution from the convective precipitation during summer is indeed slightly larger in UKESM1 compared to ECHAM-SALSA (Figure S156). This difference could be reflected in more effective summertime removalreduction in the particle mass in UKESM1. Another explanation for the more effective removal reduction of the aerosols during summertime in UKESM1 could be arising from the differences in the parametrizations of the re-evaporation of the falling droplets. In UKESM1, this process is not considered (see Sect. S2.3 and Mulcahy et al., 2020) whereas in ECHAM-SALSA evaporation of the droplets can occur and thus release the aerosols back to the atmosphere (e.g., Stier et al., 2005). During summertime, this re-evaporation could be enhanced due to higher temperatures, leading to less effective observed removal reduction of aerosols in ECHAM-SALSA compared to UKESM1. However, there can also be other explaining factors, such as location of the precipitation during travel, emissions and dry deposition, which could also indirectly cause differences between the models. Quantifying the exact processes from model parametrizations causing the differences between the observed relationships between aerosol mass and integral precipitation likely requires specific model sensitivity simulations to investigate this, thus being out of the scope of this study.

Formatted: Heading 3

#### 5 Lagrangian analysis on the effects of aqueous phase processing on aerosol chemical composition

In the analysis presented in this section, the relationship between the chemical processing occurring within clouds and fogs in the aqueous-phase is investigated. A special interest is in aqueous-phase SO<sub>4</sub> formation due to its high occurrence in the atmosphere (e.g., Ervens, 2015; Huang et al., 2019; Liu et al., 2020b). To investigate the effects on cloud processing by utilizing the Lagrangian trajectory framework, We employ a cloud proxy based on relative humidity (RH) along the trajectories—was created similar to Isokääntä et al. (2022). To this end, the history of the air mass is investigated, and if the RH exceeds 94 %, we assume the air mass is in cloud. Further, the air masses were then separated into "clear sky" in which they had no experience of clouds or precipitation during the last 24 hours, and "in-cloud" when the RH exceeded 94 % at least at one trajectory point but no precipitation events occurred during the last 24 hours (Table S7). These definitions are summarised in Table S7. Only the last 24 hours of the airmassair mass history were considered, as with longer airmassair mass histories (i.e., longer investigated time) the number of strictly in-cloud trajectories decreases due to increasing possibility for precipitation events. Sensitivity tests were conducted by adjusting both the RH limit (from 90 % to 98 %) and trajectory length (from 12h to 60h), but they did not affect our conclusions. It was found that the trajectory length adjustment has large effect on the statistical reliability of the results, hence the investigation is limited to the last 24 hours and thus also stayed consistent with the previous investigation in Isokääntä et al. (2022). This approach is applied for ERA-Interim reanalysis and for the GCM trajectories in similar manner.

Reader should also note that UKESM1, ECHAM-SALSA and ERA-Interim do not necessarily have identical definitions for RH which could impact the results. To acknowledge this, we also investigated how well the RH along the trajectories actually describes the in-cloud cases by comparing this RH-based proxy to the collocated cloud fraction data from GCMs. This analysis is presented in Sect. S6, and overall, the cloud events (number of the events and their locations at the trajectories) from both approaches were similar, leading to similar conclusions-considering aqueous phase processing of aerosols as presented in Sect. 5.1 and 5.2 below. Additionally, the The precipitation used in the classifications here is the total precipitation (including both stratiform and convective precipitation), as aqueous-phase processes are taking place no matter the cloud type. The RH data—which is used to calculate the cloud proxy—Relative humidity data is used from the HYSPLIT output instead of using raw GCM/ERA-Interim outputs with manual collocateo-location..., as RH data from This is because UKESM1 was extracted on pressure levels instead of model levels, and the latter were used in this work for the manual collocateo-location allowing consistency between other variables. The seasonal division applied here is based on the temperature, as in Sect. 4.2, to ensure sufficient statistics for the chemistry observations. To see whether transport directions and consequently the precursor emissions matter, data is divided into more clean and more polluted air masses (trajectories visiting latitudes below 60° north assigned to polluted sector as in Isokääntä et al., 2022).

In this section, the variation in the total submicron mass of different chemical species depending on the experienced conditions is first examined and discussed for the GCMs (Sect. 5.1) and reflected to observations. Then, in the next section (Sect. 5.2), a size-resolved analysis is conducted to determine whether additional insight into in-cloud processing in GCMs

could be provided.

## 5.1 Effects of in-cloud processing for total submicron aerosol mass

Trajectory frequency maps for these sectors are shown in Figure S167.

Figure 9 shows the mass concentrations of different chemical species for air masses described as "cold and polluted" (CP) for observations and the GCMs. Other air mass sectors are shown in the supplementary material (Figure \$18). The

observations shows larger SO<sub>4</sub> mass for the cloud-processed air masses, similar to the results shown in Isokääntä et al. (2022), despite the reduced data amount due to temporal harmonization with the GCMs (see Sect. 2.4). The same effect, higher SO<sub>4</sub> mass for cloud-processed air masses, is also seen for both GCMs. Both observations and GCMs show higher SO<sub>4</sub> mass concentrations for cloud-processed air masses within the "cold and polluted" (CP) sector (Figure 9), consistent with findings from Isokääntä et al. (2022). This pattern holds despite the reduced observational dataset due to temporal harmonization with the GCMs (see Sect. 2.4). Other air mass sectors are shown in the supplementary material (Figure S18).

991

992

993

994

995

996

997

998

999

000

001

002

1003

004

005

006

007

008

009

010

011

012

013

014

015

016

017

018

019

020

021

022

023

024

025

026

027

028

1029

Overall, for all presented Across all air mass sectors, both GCMs agree remarkably-well with the observations-when, considering the unavoidable expected differences in the total mass concentrations for the different chemical species. Statistically significant increases in SO<sub>4</sub> mass for in-cloud versus clear-sky air masses were found in both observations and models (p  $\leq$  0.001, Kruskal-Wallis test; Table S8), except for the warm and clean sector (Figure S17g-f), where no clear difference was observed. The increases in the SO4 masses between the clear sky and in-cloud air masses were also statistically significant for observations and both GCMs based on Kruskal-Wallis rank sum test when limit of p ≤ 0.001 is used to reject the null hypothesis (Table S8). A statistically significant increase (higher SO4 mass in in-cloud airmasses compared to clear sky airmasses) was present in all air mass sectors except for the warm and clean air masses (Figure S18g f), in which neither a significant decrease nor increase can be observed. As iIn Isokääntä et al. (2022), this may reflect limited the same observation was made, and this study speculated this would be likely due to less SO2 availability le to be oxidised in the for aqueous-phase oxidation during the warmer months in the air masses arriving from thein cleaner, warmer air masses, areas with little anthropogenic influence. Supporting this, For UKESM1, it was possible to investigate the concentrations of SO2 during the transport. T shows the lowest SO2 levels in clean sectors concentrations along the airmass trajectories are shown in Figure S19, and indeed the lowest values can be observed in the clean sectors (CC and WC: in-Figure S189e), while higher SO2 in-In contrast, both cold and warm polluted sectors (CP and WP) exhibit higher SO2 concentration along the trajectories coincideing with the largest differences in greater SO4 differences aerosol mass between clear sky and cloud processed air masses. Recently, a study on Holuhraun volcanic eruption showed that the aqueous phase oxidation rates from GCMs for SO2 to SO4 conversion provided better results than gaseous phase rates, when compared to values derived from observations (Jordan et al., 2023). This further corroborates the idea that the availability of SO2 for aqueous phase oxidation is behind the seasonal and air mass origin based differences observed between the air mass sectors in Figure 9 and Figure S18. In future climates, the SO2 in the atmosphere could increase due to more frequent and/or larger volcanic eruptions (Chim et al., 2023), thus possibly increasing the contribution of in cloud production of SO<sub>4</sub> and causing further changes in overall particle number size distributions and their chemical composition. Recent findings from the Holuhraun eruption (Jordan et al., 2023) also suggest aqueous-phase oxidation dominates SO2-to-SO4 conversion in GCMs. While future increases volcanic activity (Chim et al., 2023), could enhance SO<sub>2</sub> levels and boost in-cloud SO<sub>4</sub> production, ongoing emission controls may reduce anthropogenic SO<sub>2</sub>, potentially counteracting this effect and influencing aerosol size and composition.

Isokääntä et al., (2022) did not observe significant aqueous phase SOA (hereafter, aqSOA) formation from the observations and this has also been noted previously (Graham et al., 2020) for similar boreal forest environment as the SMEAR II studied here. Formation of SOA from gaseous precursors dominates this boreal region (see e.g., Petäjä et al., 2022), and thus distinguishing aqSOA from the total formed SOA with our methodology is challenging. For other environments, such as those where isoprene more dominant, the formation of aqSOA is a significant source for total SOA

Formatted: Subscript

burden (e.g., Lamkaddam et al., 2021). Also biomass burning emissions have been identified as a potential source for aqSOA (Gilardoni et al., 2016; Wang et al., 2024).

The observations shown here do not exhibit statistically significant differences for OA between the clear sky and in-cloud airmassair masses in any of the sectors. The median mass of OA in ECHAM-SALSA is larger for the in-cloud airmassair masses for the cold and polluted sector (Figure 9Figure 9c and Table S8), but no other sectors exhibit statistically significant differences. However, this difference in the OA mass in the cold and polluted sector is unlikely due to formation of aqSOA, as the simulations employed in this study here did not explicitly model the formation of SOA. UKESM1 displays larger differences in the OA mass, in which most are also statistically different. However, the same applies as for ECHAM-SALSA, i.e., the model simulations do not include the formation of SOA, and thus the differences must arise from other affecting factors. Both GCMs employ CMIP6 emission datasets as noted in the model setup for AeroCom Phase III GCM Trajectory Experiment, and thus the differences observed here unlikely arise from varying emissions. One should also keep in mind that the representations of OA in the GCMs might differ, and especially their relationship with temperature, relevant driver for SOA formation in general, has been shown to exhibit large structural uncertainties between the GCMs (Blichner et al., 2024).

Isokääntä et al., (2022) did not observe significant aqueous-phase SOA (hereafter, aqSOA) formation from the observations and this has also been noted previously (Graham et al., 2020) for similar boreal environment. Formation of SOA from gaseous precursors dominates this boreal region (see e.g., (Petäjä et al., 2022), and thus distinguishing aqSOA from the total formed SOA with our methodology is challenging. For isoprene-dominated environments, the formation of aqSOA is a significant source for total SOA burden (e.g., Lamkaddam et al., 2021). Also biomass burning emissions have been identified as a potential source for aqSOA (Gilardoni et al., 2016; Wang et al., 2024).

It was reported earlier that the observations also suggested increase in the mass fraction of SO<sub>4</sub> when the airmassair masses had been exposed to in-cloud conditions long enough (Isokääntä et al., 2022). To investigate whether similar behaviour could be observed for the GCMs, we calculated the total time spent under the influence of non-precipitation clouds from the 96h long trajectories. Figure 10 demonstrates slight increases in the mass fraction of SO<sub>4</sub> with increasing time spent in non-precipitating clouds for both GCMs. This, however, is somewhat affected by the data size. If inspecting the GCM data which is temporally harmonised to the observations (Figure 10Figure 10a-b), the conclusion is not as obvious compared to the case were inspecting all available GCM data (Figure 10Figure 10c-d). This highlights the importance of long enough GCM simulations needed in this type of Lagrangian analysis utilizing single particle air mass trajectories unless ensemble trajectories are utilised.

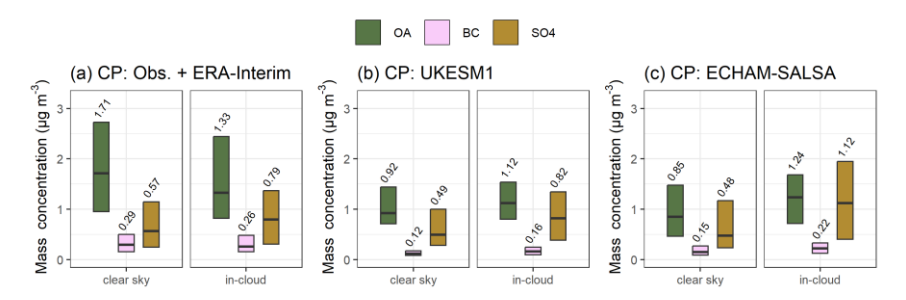


Figure 99 Median (black horizontal lines and numerical values) particle mass concentrations at SMEAR II with 25th–75th percentiles (boxes) for OA, eBC, and SO4 for the cold and polluted (CP) airmassair mass sector. The experienced conditions by the air mass are denoted as clear sky and in-cloud (non-precipitating). Subplots include (a) SMEAR II + ERA-Interim, (b) UKESM1 and (c) ECHAM-SALSA.

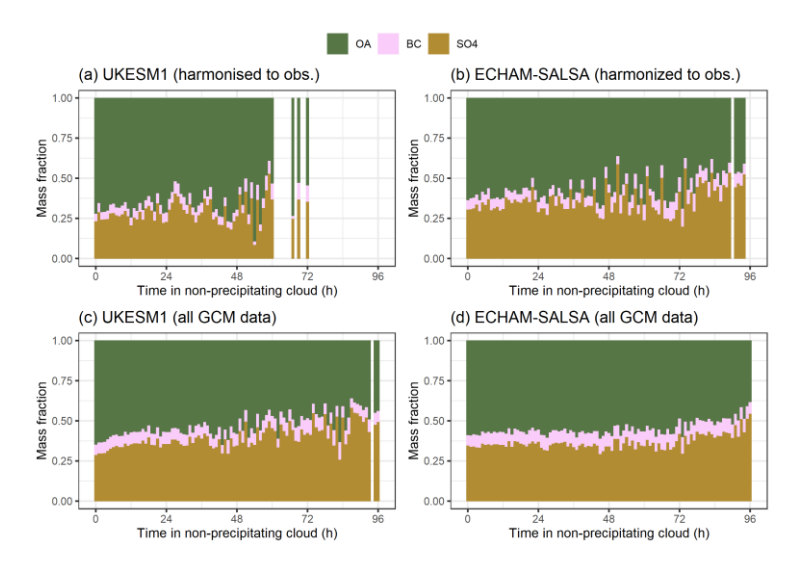


Figure  $\underline{1010}$  The mass fractions of OA, SO4, and BC for the more polluted air masses as a function of time spent in in non-precipitating cloud. The top row (a-b) shows the temporally harmonised data and bottom row displays the GCM data without harmonization. The figure shows mass fractions derived from median concentrations for each 1-hour bin.

# ${\bf 5.2~Effects~of~in\text{-}cloud~processing~for~size\text{-}resolved~aerosol~mass}$

060

To see whether the observed in-cloud formed SO<sub>4</sub> mass in the GCMs (Figure 9Figure 9b-c) is contributing to same particle sizes as in the observations reported in Isokääntä et al. (2022), the analysis was repeated here for the GCMs. The observations indicated SO<sub>4</sub> mass originating from aqueous-phase processes is mostly contributing to particles with diameters of 200-1000 nm—(Figure S20 and Isokääntä et al., 2022). Figure 11Figure 11 shows the particle mass concentrations for various size classes derived from the PNSDs from the GCMs for the clear sky and cloud processed air masses for the cold and polluted sector. The three other sectors for the GCMs are shown in Figure S1921,

and Table S9 shows the results for the GCMs from the statistical significance testing between the clear sky and in-cloud groups within each size class. Compared to observations, UKESM1 data (Figure 11 Figure 11 a and Figure S21 for the rest of the sectors 19) implies the mass increase seems to be mostly distributed to bins with  $d_p = 100$ -350 nm and up to 600 nm in the cold and polluted and cold and clean sectors. This is likely due to UKESM1 having large concentrations of particles in general within this size range (see e.g., Figure 2Figure 1d). Like the observations, UKESM1 does not exhibit any mass increases for any of the size bins in the warm and clean sector (Figure S 1922e), being in line with no observed increase in the SO<sub>4</sub> mass in the same sector (WC) between the clear sky and cloud processed air masses (Figure S128h).

089

ECHAM-SALSA (Figure 11Figure 11b and Figure S21 for the rest of the sectors19), exhibits increased mass concentrations for sizes starting from  $d_p = 50$  nm (only in cold and polluted sector) up to 1700 nm, depending on the sector. The largest bin here in ECHAM-SALSA might also be influenced by  $d_p = 1-1.7 \mu m$  particles, which are neither considered in UKESM1 nor in the observations when inspecting the chemical components (see Sect. 2.4.2). Like UKESM1, ECHAM-SALSA also does not exhibit mass increases for any of the size bins for the warm and clean sector (Figure S21f).

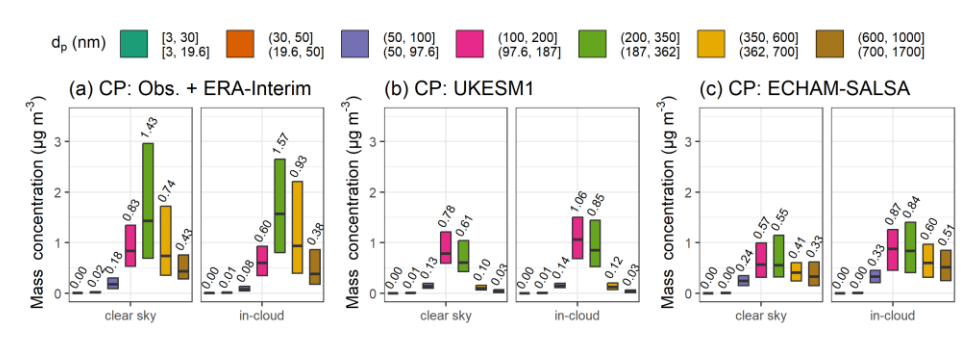


Figure 1114 Median (black horizontal lines and numerical values) particle mass concentrations with 25th-75th percentiles (boxes) for selected size bins for (a) observations with ERA-Interim, (b) UKESM1 and (cb) ECHAM-SALSA for the cold and polluted (CP sector). For the latter, the native size bins are shown (bottom row of the legend). The experienced conditions by the air mass are denoted as clear sky and in-cloud (non-precipitating).

An advantage of the GCMs used in this study is their provision of size-resolved chemical composition, shown as mass fractions in Figure S202. For UKESM1, increase in the soluble  $SO_4$  in the accumulation mode can be observed (Figure S202a). Due to the model structure, however, the accumulation mode itself consist of a large spread of particle sizes ( $d_p = 100-1000$  nm), i.e., internally mixed aerosols with external size modes, thus not providing additional information to our PNSD based analysis. For ECHAM-SALSA, the original sectional bins can be inspected (Figure S202c) thus corresponding to the PNSD bins presented in Figure 11Figure 11b. All size bins that exhibited mass increases in Figure 11Figure 11b also exhibit higher mass fraction for  $SO_4$  in Figure S202c.

The observed changes in particle number size distributions (Figure 11) reflect the actual model parameterizations. In UKESM1, SO<sub>4</sub> produced via aqueous-phase chemistry is allocated to the soluble accumulation mode (dp > 100 nm) and coarse mode (dp > 500 nm) (Mann et al., 2010), with the results here showing increases in the 100–600 nm range. In ECHAM-SALSA, aqueous-phase SO<sub>4</sub> is distributed across soluble size bins spanning 50–10000 nm (2a bins; see Table S3, Bergman et al., 2012), with sector-dependent mass increases observed between 50–1700 nm. Overall, in the GCMs

the changes in the particle chemistry due to cloud processing (Sect. 5.1) are well reflected in the changes in the particle number size distributions. The analysis presented here accurately reflects the actual model parametrizations. In UKESM1, the SO<sub>4</sub> produced from aqueous phase chemistry is distributed to soluble accumulation ( $d_p > 100$  nm, Table S2) and coarse modes ( $d_p > 500$  nm) (Mann et al., 2010), and results shown here indicated size range of  $d_p = 100$ -600 nm. In ECHAM SALSA, the aqueous phase SO<sub>4</sub> is distributed to soluble bins having diameters between  $d_p = 50 - 10000$  nm (2a bins, see Table S3, Bergman et al., 2012), and mass increases were observed for  $d_p = 50$ -1700 nm, depending on the sector. In terms of aqueous-phase oxidation of SO<sub>2</sub> both GCMs have similar parametrizations, and for example, oxidation of SO<sub>2</sub> by ozone (O3) and hydrogen peroxide (H<sub>2</sub>O2) is considered in both (Bergman et al., 2012; Hardacre et al., 2021).

### 6 Conclusions and outlook

In this study we investigated the effects of stratiform precipitation (wet removal) and clouds (aqueous-phase oxidation) on sub-micron sized aerosols along airmassair mass trajectories. We studied (Two global climate models—UKESM1 and ECHAM-SALSA—in a manner consistent towere analysed using a Lagrangian framework consistent with Isokääntä et al. (2022) by employing the Lagrangian framework which can now be, now being seamlessly applicableied to the GCMs (Kim et al., 2020). Our geographical study area focused on focus was the SMEAR II station in Hyytiälä, Finland, and the surroundings, thus being representative of the boreal environment.

Our first objective was to investigate whether the trajectory-based relationships between aerosols mass, number and precipitation vary between the observations and the two GCMs. For aerosol mass, the derived removal for observations resided in fell between the GCMs for both summer and wintertwo models across seasons. In contrast, aerosol number showed stronger divergence: while ECHAM-SALSA and observations indicated minimal reduction, UKESM1 exhibited significant loss in particle number via precipitation, likely due to a lack of small particles in the model. Supplementary analysis comparing a wider ensemble of GCMs indicated that these two models were broadly representative, with their aerosol-precipitation relationships generally falling near the middle of the inter-model spread. For aerosol number, greater differences were observed. While both the observations and ECHAM-SALSA indicated little to no removal, UKESM1 exhibited evident removal. This strong removal of particle number in UKESM1 is likely attributable to the absence of small particles, which were present in the observations and ECHAM-SALSA. RemovalReductions of the different chemical species, in organic aerosol (OA), sulfate (SO4) and black carbon (BC), was also inspected, and the aerosol-precipitation patterns followed the ones presented for also followed the same general trends as total aerosol-mass, despite more vague seasonal separationalthough with weaker seasonal differences. Our use of normalized submicron mass and number as a function of accumulated precipitation proved effective in comparing removal across models, though it lacks detail on particle size evolution—an important topic for future work.

Our methodology used here of inspecting normalized quantities of total submicron aerosol mass and number as a function of accumulated precipitation is an effective way for evaluating the removals in the GCMs since it aims to minimize the differences due to different aerosol number size distributions between the GCMs. However, it does have its limitations as it only gives the overall effect of precipitation on aerosols. Further studies in which the PNSDs are inspected in more detail are essential.

As suggested by earlier studies, the process by which and erosols activation into cloud droplets followed by removal via precipitation rainout, is likely appears to be the dominant removal process, on average, also in this study being in line with earlier work. UKESM1 results further supported this showing nucleation followed by rainout as the largest contributor. This was, for example, supported by inspecting the contribution of different wet removal processes from UKESM1 from which nucleation followed by rainout showed largest contribution. The seasonal differences in the observed removals within the GCMs were evaluated further by inspecting key variables, such as, number of potential cloud condensation nuclei (N<sub>80</sub>) and sub-grid scale vertical velocities (updraughtsupdraught velocities), controlling aerosol activation into cloud droplets. The seasonal differences we observed in these variables, along with changes in particle chemistry during the transport, were found to be consistent with the seasonality of the aerosol-precipitation relationships. Further inspection of the r The relationship between activated fractions and updraught velocities shows opposite seasonal patterns in the GCMs: UKESM1 has a stronger summer correlation, while ECHAM-SALSA's is stronger in winter, though its seasonal variation is smaller overall elationship between activated fractions and updraughts

Formatted: English (United States)

revealed that the seasonality of strength of this relationship is opposite when the GCMs are compared—UKESM1 exhibits stronger relationship in summer and ECHAM SALSA in winter, the seasonal differences in the latter being significantly smaller—than—in former. This behaviour further explains the—observed differences between the aerosol-precipitation relationships in which ECHAM-SALSA showed similarity to observations. We hypothesize that UKESM1's pattern may stem from the absence of boundary layer nucleation, resulting in fewer small particles during summer. This emphasizes the need for better representation of particle number size distributions (PNSDs) in GCMs. We suggested, among other things, that the opposite behaviour in UKESM1 could be affected by the missing boundary layer nucleation and thus influenced by the lack of small aerosols in summertime and thus ultimately converging to the representation of PNSDs correctly in GCMs. However, further work is needed to elucidate which of the differences in the GCMs parametrizations are influencing the results we observe here, as many of the processes are interconnected; see, for example, the work from Proske et al. (2022, 2023, 2024) and Schutgens and Stier (2014)<sub>3</sub>

In addition to comparing these two GCMs, the representativeness of these models was inspected by simple comparison of the aerosol precipitation relationships and rainfall rates among a larger group of GCMs available from AeroCom GCMTraj simulations. Among these GCMs, both UKESM1 and ECHAM SALSA were relatively close to the ensemble mean i.e., they are not representing the extremities. More work is warranted on investigating these other GCMs in more detail, for example by evaluating how the parameters controlling activation, those also inspected in this work, evolve during airmass transport. Additional insights could also be obtained by investigating other related parameters, such as effective radius of cloud droplets and autoconversion rates, to be able to further examine the patterns we observed in this study.

Earlier studies (Isokääntä et al., 2022; Khadir et al., 2023) have noted that surface precipitation data, commonly used in trajectory analyses, may not accurately reflect precipitation experienced by air masses at trajectory height. Here, we used vertically resolved precipitation from UKESM1 and found that surface precipitation serves as a good proxy in this environment, where trajectories largely remain within the mixed layer and stratiform precipitation dominates. However, this analysis only considered liquid precipitation and may not apply to regions where convective precipitation is more prevalent. In such environments, the vertical distribution, intensity, and frequency of precipitation could differ substantially, potentially altering the accumulated wet removal along trajectories. Therefore, while our results are representative of boreal regions with stratiform precipitation, further work is needed to assess how applicable they are to regions with different precipitation regimes, have brought up the fact that the precipitation data, which is usually available for trajectory analysis, depicts precipitation at the surface and is thus not exactly descriptive of the experienced precipitation by the airmass at the trajectory height. From UKESM1, precipitation data can also be extracted at the model levels and in this study, we additionally exploited this possibility. We showed that the precipitation at the surface is a good proxy for this environment, in UKESM1, for the actual experienced precipitation by the airmass when the airmasses mostly stay within the mixed layer and are thus below the clouds. However, our comparison was only limited to liquid precipitation. In addition, our analysis is focused on a geographical area in which stratiform precipitation dominates. The situation is likely different in places where convective precipitation is more frequent. Therefore, future Lagrangian based GCM evaluation studies should include more work on areas where convective precipitation might dominate, also in relation to whether the effects on aerosols via accumulated precipitation are similar compared to stratiform precipitation presented here.

Field Code Changed

Field Code Changed

Formatted: English (United Kingdom)

Our second objective was to investigate whether the GCMs exhibit similar increase in sulfate mass due to in-cloud production as the observational data, and whether these observed effects are in line with the model parametrizations. Bothdata. Both GCMs exhibited statistically significant difference in the SO<sub>4</sub> mass when airmassair masses with only clear sky experience were compared to in-cloud processes airmasses. The SO<sub>4</sub> mass was larger for the cloud processed airmassair masses for all other airmassair mass sectors (based on temperature and direction) except the warm and clean airmassair masses, where GCMs showed no significant difference between clear sky and in-cloud airmassair masses. These results agree well with our earlier study utilizing a slightly larger observational data sewere consistent with earlier workt (Isokääntä et al., 2022) from the same site. Availability of the SO<sub>2</sub> to be oxidised is likely determining whether we see in-cloud production of SO<sub>4</sub>, and from UKESM1 this was further supported by the inspected—SO<sub>2</sub> concentrations and their seasonality. The size-resolved analysis reflected the model parametrizations, well, as expected, the aqueous-phase SO<sub>4</sub> being mostly distributed in the larger aerosol sizes. Future studies involving GCMs could examine the contributions from gas-phase and aqueous-phase SO<sub>4</sub>-formation in more detail within the Lagrangian framework, by investigating how these quantities evolve during the transport.

As expected based on Isokääntä et al. (2022), the reduced observations here alsowe did not indicate observe significant aqueous-phase SOA formation. This is likely due to the studied environment (boreal forest), and has also been noted previously (Graham et al., 2020) for similar boreal forest environment. However, some increases in OA mass were seen in the GCMs despite the fact that aqSOA formation was not explicitly modeled, possibly reflecting other processes or model inconsistencies. The GCMs, however, exhibited inconsistencies, and in some cases increases in the OA mass could be observed for cloud processed airmasses. The GCM simulations utilized in this study, however, did not explicitly model the formation of SOA and thus also not aqSOA, hence these differences must be due to other reasons. A recent study from Blichner et al. (2024) also pointed out the large differences between GCMs concerning their OA-temperature relationships, which could also contribute to the discrepancies observed here.

Overall, both GCMs reproduced the observed exponential decrease in aerosol mass with increasing precipitation and showed similar cloud-processing behaviour for SO4. Yet key seasonal differences remain, especially in aerosolprecipitation relationships and their underlying drivers. A primary model bias identified in this study is the difference in aerosol number size distributions compared to observations, particularly the underrepresentation of small particles in UKESM1. Our results suggest that discrepancies arise more from differences in aerosol size distributions and updraught velocities than from the wet removal parametrizations themselves. These variables also affect activated fractions and cloud interactions, and they are shaped by processes beyond the 4-day analysis window. Overall, the GCMs show similar behaviour as the observations considering the exponential decrease of total particle mass as a function of the accumulated precipitation along the trajectories. Also, the effects of cloud processing agree between observations and GCMs when SO+ is considered. However, differences arise when different seasons are inspected, especially in the aerosol-precipitation relationships and their drivers. In general, our analysis suggests the wet removal parametrizations within these models are sufficient, and the differences are more likely to arise from differences between the aerosol particle number size distributions and updraughts. The size distributions are not only affected by the wet removal and cloud processing during the air mass trajectory, but also due to modifying the activated fractions which further affect cloud properties. The starting size distributions can also be impacted by various processes further away than the investigated 4 days, which can differ between the GCMs.

Further work on acrosol-precipitation relationships is still critical, and work on how the acrosol size distribution evolves during transport due to various sink and source processes is especially warranted. Despite the required computational effort, utilizing larger group of GCMs is useful on untangling the diverse outcomes observed in the acrosol-precipitation relationships, and the authors pose this as an important future work.

# 1232 <u>7 Outlook</u>

 While our results show encouraging agreement between observations and GCMs in overall aerosol–precipitation relationships, key differences—especially related to seasonality and aerosol number—highlight the need for further work. Future studies should investigate the evolution of aerosol size distributions along air mass trajectories in more detail and better disentangle gas-phase and aqueous-phase sulfate formation. Expanding analyses to regions with dominant convective precipitation is also important, as the findings here are limited to stratiform, liquid-phase conditions typical of boreal environments. Including a wider range of GCMs, despite the computational demands, would help clarify the structural causes behind the differences observed. Together, these efforts are essential for improving the representation of aerosol–cloud–precipitation interactions in climate models. Future studies involving GCMs could examine the contributions from gas phase and aqueous phase SO<sub>3</sub> formation in more detail within the Lagrangian framework, by investigating how these quantities evolve during the transport. Further work on aerosol precipitation relationships is still critical, and work on how the aerosol size distribution evolves during transport due to various sink and source processes is especially warranted. Despite the required computational effort, utilizing larger group of GCMs is useful on untangling the diverse outcomes observed in the aerosol precipitation relationships, and the authors pose this as an important future

Formatted: Heading 1

### Appendix A

The lack of vertical resolution in the precipitation data obtained from ERA-Interim reanalysis or Global Data Assimilation System (GDAS, (http://ready.arl.noaa.gov/archives.php, last access: 3.2.2024) in studies using Lagrangian approaches is now being recognised (Dadashazar et al., 2021; Isokääntä et al., 2022; Khadir et al., 2023). Unfortunately, vertically resolved precipitation data, for example, from reanalysis datasets or GCMs, with high enough time resolution to be useful for trajectory models, is not a commonly provided diagnostic. For UKESM1, however, vertically resolved precipitation data is athis diagnostic-that can be extracted from the model run. Here, we have conducted a comparison between the vertically resolved and surface precipitation data along the airmassair mass trajectories to investigate how well the surface precipitation describes the actual experienced precipitation by the airmassair mass. Only liquid (stratiform) precipitation is inspected, as vertically resolved snowfall was not included in the variable extraction with high enough vertical resolution for this model run.

We started our investigation by inspecting first inspected the relationship between the normalized particle mass and number with the accumulated stratiform precipitation, similar to what is shown in Figure 4.5. This assessed whether aerosol-precipitation relationships differ between surface and vertically resolved precipitation, to see whether the aerosol precipitation relationships are different for the different precipitation types (precipitation at the surface vs. vertically resolved precipitation). This analysis, dDisplayed in Figure A1, the results indicates the effects of stratiform precipitation at the height of the airmassair mass are similar to the effects of stratiform precipitation at the surface. This is likely related to the average altitude of the airmassair masses, as for SMEAR II they tend to travel well below the top of boundary layer.

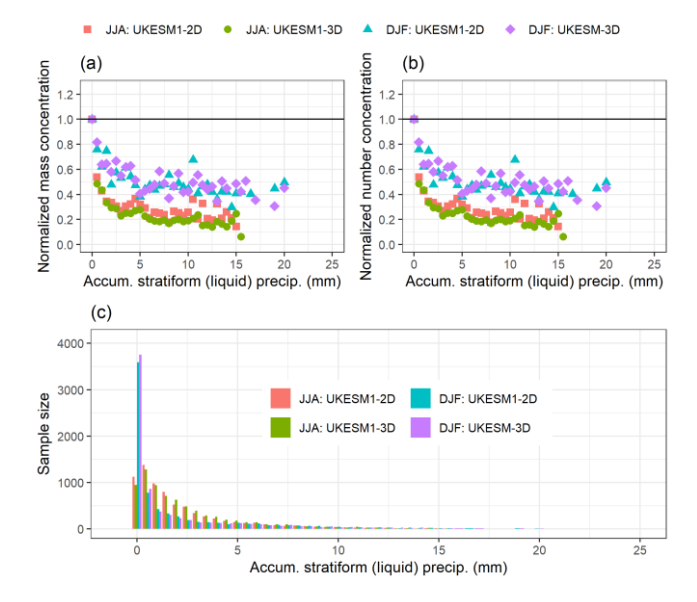


Figure A1 Normalized total ( $d_p$  = 3-1000 nm) particle mass (a) and number (b) at SMEAR II for summer (JJA) and wintertime (DJF) as a function of 0-25 mm of accumulated liquid stratiform precipitation along the  $\frac{96 \text{ hour} 96}{\text{hour}}$  long  $\frac{1}{\text{airmassair mass}}$  (referred as 3D) and at the surface

(referred as 2D) for UKESM1. The coloured points show the median values for each 0.5 mm bin of accumulated precipitation when the number of  $\frac{data-rowstrajectories}{data-rowstrajectories}$  in the bin was 10 or larger. The sample size for the corresponding bins is shown in (c).

To investigate—in more detail whether the height of the airmassair mass plays a role, as speculated in Isokääntä et al. (2022), the airmassair mass trajectory altitudes were—first clustered with Kmeans (e.g., Hartigan and Wong, 1979) and 3 clusters with distinct height profiles were selected for further analysis. Clustering each season separately provided similar height profiles as clustering of the whole data, and thus the latter approach is presented—here.

Figure A2 shows the median altitudes of the clusters and the corresponding mean stratiform rainfall rates. Overall, the mean rainfall rates show similar values despite the precipitation diagnostic. In the low-altitude cluster (Figure A2d), overall highest rainfall rates (mean over all trajectories and hours for surface precipitation,  $\sim 0.033 \text{ mm h}^{-1}$ ) are observed. In the mid-altitude cluster, rainfall rates are smaller ( $\sim 0.016 \text{ mm h}^{-1}$ ) compared to the low-altitude cluster, and in the high-altitude cluster, the rainfall rates are the smallest ( $\sim 0.010 \text{ mm h}^{-1}$ ). In the high-altitude cluster (Figure A2f) more differences emerge between the two precipitation types, especially afar from SMEAR II.

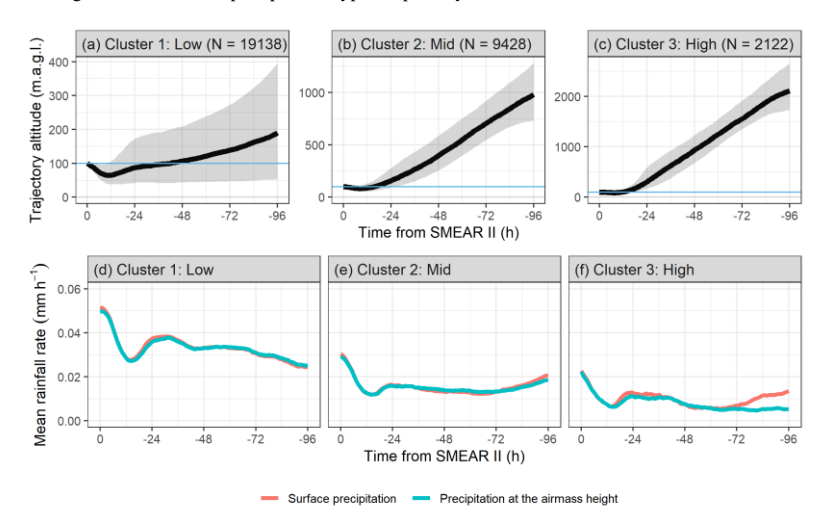


Figure A2 Clusters based on airmassair mass trajectory altitudes for UKESM1. In (a)-(c) the black lines show median trajectory altitude as a function of time from SMEAR II and 25th to 75th percentiles are shown with the shaded area. The used arrival height at SMEAR II given to HYSPLIT is indicated with blue horizontal line. The corresponding mean rainfall rates are shown in (d)-(f). Clusters are named based on the maximum altitude the trajectory has resided during the last 4 days. Note the different y-axis limits in subplots (a)-(c).

Each cluster was then further separated by season for more detailed analysis. The median altitudes, if inspected separately for each season, are nearly identical between the seasons within each cluster, and thus not shown here. Figure S2123 shows the differences between the mean liquid rainfall rates between surface and vertically resolves stratiform precipitation (positive difference indicating the rainfall rates at the surface are higher) for each cluster and each season.

During autumn (SON) the two approaches for the precipitation exhibit observable differences only in the high-altitude cluster, where the surface precipitation shows some overestimation of the actual experienced precipitation by the

airmassair mass with increasing trend when moving farther away from SMEAR II. This could imply that the airmassair mass has spent some time above or inside the precipitating cloud, as also the airmassair mass altitude increases when moving away from the station (Figure A2a-c). During summer (JJA), all clusters mostly show precipitation at the airmassair mass height being larger than the surface precipitation, expect in the high-altitude cluster (Figure S2123c) 72 to 96 hours before arrival to SMEAR II. As the temperatures during summer are higher than in other seasons, this could be indication of evaporation as the surface precipitation in UKESM1 includes only precipitation that reaches the surface i.e., it is not column integrated. During spring (MAM) and winter (DJF) the surface precipitation shows small overestimation at some points along the trajectories, and the differences are largest at the high-altitude cluster—where, however, the rainfall rates are very small overall (see Figure A2f) for both precipitation types.

### 1305 Appendix B 306 In this work, all the model simulations follow AMIP style runs following the experiment setup for AeroCom phase III 307 GCMTraj experiment (see also Aerosol GCM Trajectory (GCMTraj) | AeroCom, 2024). Therefore, only summaries of 308 the models are given here. 309 ECHAM-HAM 1310 ECHAM6.3 HAM2.3 (referred as ECHAM HAM) is a global aerosol-climate model consisting of ECHAM (Stevens et 311 al., 2013) coupled with the Hamburg Aerosol Model HAM (Tegen et al., 2019). In difference to ECHAM SALSA, 1312 ECHAM-HAM uses the modal acrosol model M7 as its microphysical core (Stier et al., 2005; Vignati et al., 2004). 313 ECHAM HAM is run at a horizontal resolution corresponding approximately to 1.875° x 1.875° (latitude longitude) and 1314 47 vertical levels extending up to 0.01 hPa. 315 M7 has four log-normal modes for soluble (nucleation, Aitken, accumulation, coarse) and three for insoluble (Aitken, 1316 accumulation, coarse) aerosol particles. Sulfate is included in all seven modes, black carbon and primary organic aerosol 317 in all modes except the nucleation mode and insoluble accumulation and coarse modes. Sea salt and mineral dust are 318 traced in soluble accumulation and coarse modes and mineral dust also in insoluble accumulation and coarse mode. 1319 The wet scavenging schemes in ECHAM HAM are relatively similar to ECHAM SALSA (see Sect. S2). In cloud 1320 impaction scavenging is dependent on the wet particle size and follows Croft et al. (2010) and scavenging via droplet 1321 activation, which follows Abdul Razzak and Ghan (2000). The in-cloud scavenging scheme considers scavenging in 322 different cloud types, distinguishing between stratiform and convective clouds and warm, cold, and mixed phase clouds. 1323 Below clouds particles are scavenged by rain and snow using a size-dependent below-cloud scavenging scheme (Croft et 1324 al., 2009). Scavenged particles can also be resuspended in the atmosphere, as in ECHAM SALSA, when precipitation 1325 evaporates (Stier et al., 2005). 1326 ECHAM-HAM-P3 1327 ECHAM6.3-HAM2.3-P3 (referred as ECHAM-HAM-P3) is the combination of the ECHAM (Stevens et al., 2013), the 328 Hamburg Aerosol Module (Tegen et al., 2019) and Perturbed Particle Physics (P3) ice cloud microphysics scheme 1329 (Dietlicher et al., 2018, 2019). The P3 configuration of ECHAM-HAM offers better constrained conversion rates and 1330 prognostic ice sedimentation, as well as a more realistic representation of mixed phase and cirrus cloud cover (Dietlicher 331 et al., 2019). The simulations were run with a horizontal resolution of 1.875° x 1.875° (latitude longitude) and with 47 1332 vertical levels extending up to a 0.01 hPa. 1333 Description of aerosols and wet scavenging processes in ECHAM-HAM-P3 are identical to ECHAM-HAM. 1334 CAM5 1335 The Community Atmosphere Model version 5.3 (CAM5.3, hereafter only CAM5, see also Neale et al., 2012) is the 1336 atmospheric component of the Community Earth System Model (CESM, Hurrell et al., 2013). CAM5 is configured with

at a spatial resolution of 1.9°x2.5° (latitude longitude), and 30 vertical layers from the surface to 3.6 hPa (corresponding

1337

1338

approximately to 40 km).

339	The aerosols in CAM5 (Liu et al., 2016) are distributed to four lognormal modes (i.e., Aitken, accumulation, coarse, and
340	primary carbon modes). The model predicts aerosol species including sulfate, black carbon, primary organic matter,
341	secondary organic aerosol, mineral dust, and sea salt.
342	The aerosol wet scavenging and convective transport in the model are improved based on Wang et al., (2013) on top of
343	the default CAM5.
344	NorESM
345	The Norwegian Earth System Model intermediate version (NorESM1.2; Kirkevåg et al., 2018) is based on version 1.2 of
346	the CESM (Hurrell et al., 2013) and uses the atmospheric model CAM5.3 Oslo. CAM5.5 Oslo is an updated version of
347	the Community Atmospheric Model version CAM5.3 (Liu et al., 2016; Neale et al., 2012). The ocean, land, and sea ice
348	models used are the Bergen version of the Miami Isopycnic Co-ordinate Ocean Model (MICOM) (Bentsen et al., 2013),
349	Community Land Model (CLM) 4.5 and CICE4 respectively. The model has 30 vertical levels and has a horizontal
350	resolution of 1.9° x 1.25° (latitude longitude).
351	CAM5.3-Oslo has its own aerosol module, OsloAero (Kirkevåg et al., 2018), which has 21 aerosol tracers distributed
352	among six species. These species include sulfate, secondary organic aerosol, black carbon, organic matter, mineral dust
353	and sea salt. OsloAero also includes a general chemical solver (CAM Chem) and a standardized chemical code
354	preprocessor (MOZART; Emmons et al., 2010).
355	Wet scavenging includes in-cloud scavenging (formation of cloud droplets by impaction and nucleation) and below-cloud
356	scavenging (wet removal of aerosols by precipitation) (Kirkevåg et al., 2018). The aerosol activation scheme follows
357	Abdul Pazzak and Ghan (2000).

# Data availability Raw observational data were collected by INAR, University of Helsinki. Field data (particle number size distributions and black carbon) are freely available from https://smear.avaa.csc.fi/download (last access: 20 February 2022; Ministry of Education and Culture of Finland and CSC, 2022). The ACSM data on aerosol composition are freely available from the EBAS database at http://ebas.nilu.no/ (last access: 20 February 2022; NILU, 2022). The pre-processed observational data, ERA-Interim and GCMs trajectories along with the eollocateo-located variables used in this study will be made openly available in Zenodo upon acceptance.can be found from (Talvinen et al., 2025b).

## 1366 Code availability

1367

1370

1373

1385

1386

1387

- Data analysis was conducted in R statistical software (R version 4.2.0, R Core Team, 2019) and Python (version 3.10.4),
- and colour maps for the figures considering colour vision deficiencies were inspired by Crameri et al., (2020).
- The scripts used for the analysis and to reproduce the main findingsplotting both in R and python will be made openly
  - available in Zenodo upon acceptancecan be found from (Talvinen et al., 2025a).
- Python scripts for the data conversion (GCM output into ARL) and collocatco-location of the GCM and reanalysis data
- variables to the trajectories can be obtained from DGP.

### Author contribution

- 1374 DGP and AV proposed the study. ST, DGP and AV designed the research questions. ST had the lead role in data analysis
- 1375 with supporting contribution from PK, DGP, ET and RC. The modelling framework to calculate trajectories from GCM
- 1376 meteorological fields was conceived and performed by DGP with support from ZK and JT. The development and
- 1377 application of this framework to the AeroCom GCMTraj model submissions was performed by PK with support from
- 1378 DGP. Model simulations and data submissions were performed by ET, DGP, TK, EH, HK, TK, DN, DWP, YY, JZ and
- 1379 SK. UKESM1 model simulation configuration was supported by AS, and ZK supported the processing of ERA-Interim
- 1380 reanalysis data. HYSPLIT trajectories were calculated by PK and the eollocatco-location scripts were developed by PK
- with supporting contribution from DGP, ET, ST and RC. CollocatCo-location of GCM data and ERA-Interim
- precipitation to the trajectories were performed by ST. Results were interpreted by ST, DP and AV with supporting
- 1383 contribution from all co-authors. The manuscript was written by ST with supporting contribution from DP. All co-authors
- 1384 commented, edited and gave feedback on the manuscript.

# Competing interests

At least one of the (co-)authors is a member of the editorial board of Atmospheric Chemistry and Physics.

### Acknowledgements

- 1388 We acknowledge use of the Monsoon2 system, a collaborative facility supplied under the Joint Weather and Climate
- 1389 Research Programme, a strategic partnership between the UK Met Office and the Natural Environment Research Council.
- 1390 We also thank all the people responsible for the development of UKESM1 and ECHAM-HAM-SALSA. The ECHAM-

1392	Forschungszentrum Julich, University of Oxford, the Finnish Meteorological Institute and the Leibniz Institute for
1393	Tropospheric Research and managed by the Center for Climate Systems Modeling (C2SM) at ETH Zurich.
1394	We thank technical and scientific staff from SMEAR II station.
1395	DGP would like to extend personal thanks to Ben Johnson and Andy Jones, who provided support for the configuration
1396	of the UKESM1 simulations performed as part the AeroCom GCM Trajectory experiment on which these simulations are
1397	based. DGP also wishes to thank Hamish Struthers who supported preliminary testing of CAM simulation output during
1398	the development of the coding framework to convert GCM fields into the required format for trajectory calculations, and
1399	Peter Tunved for valuable input and discussions during the development of this framework.
1400 1401	We also wish to thank Eliza Duncan from the valuable input, technical help and discussions during the development of this work.
1.01	
1402	Financial support
1403	This work has been supported by European Union's Horizon 2020 research and innovation programme FORCeS (Grant
1404	Agreement No. 821205), Horizon Europe programme via project CERTAINTY (Cloud-aERosol inTeractions & their
1405	impActs IN The earth sYstem, Grant Agreement No. 101137680) and by the project CleanCloud (Grant agreement No.
1406	101137639).
1407	This work has also received support from the Academy of Finland (grant No. 317373 and 317390), Academy of Finland
1408	Flagship funding (grant No. 337550) and the Academy of Finland competitive funding to strengthen university research

profiles (PROFI) for the University of Eastern Finland (grant No. 325022 and 352968).

HAMMOZ model is developed by a consortium composed of ETH Zurich, Max Planck Institut fur Meteorologie,

1391

### 1410 References

- 1411 Aalto, P., Hameri, K., Becker, E., Weber, R., Salm, J., Makela, J. M., Hoell, C., O'Dowd, C. D., Karlsson, H., Hansson,
- 1412 H. C., Vakeva, M., Koponen, I. K., Buzorius, G., and Kulmala, M.: Physical characterization of aerosol particles during
- 1413 nucleation events, Tellus B Chem. Phys. Meteorol., 53, 344–358, https://doi.org/10.1034/j.1600-0889.2001.530403.x,
- 1414
- 1415 Andronache, C.: Estimated variability of below-cloud aerosol removal by rainfall for observed aerosol size distributions,
- 1416 Atmos Chem Phys, 3, 131-143, https://doi.org/10.5194/acp-3-131-2003, 2003.
- 1417 Archibald, A. T., O'Connor, F. M., Abraham, N. L., Archer-Nicholls, S., Chipperfield, M. P., Dalvi, M., Folberth, G. A.,
- Dennison, F., Dhomse, S. S., Griffiths, P. T., Hardacre, C., Hewitt, A. J., Hill, R. S., Johnson, C. E., Keeble, J., Köhler, 1418
- 1419 M. O., Morgenstern, O., Mulcahy, J. P., Ordóñez, C., Pope, R. J., Rumbold, S. T., Russo, M. R., Savage, N. H., Sellar,
- 1420 A., Stringer, M., Turnock, S. T., Wild, O., and Zeng, G.: Description and evaluation of the UKCA stratosphere-
- 1421 troposphere chemistry scheme (StratTrop vn 1.0) implemented in UKESM1, Geosci Model Dev, 13, 1223-1266,
- https://doi.org/10.5194/gmd-13-1223-2020, 2020. 1422
- 1423 Bauer, S. E., Tsigaridis, K., Faluvegi, G., Nazarenko, L., Miller, R. L., Kelley, M., and Schmidt, G.: The Turning Point
- 1424 of the Aerosol Era, J. Adv. Model. Earth Syst., 14, e2022MS003070, https://doi.org/10.1029/2022MS003070, 2022.
- 1425 Bellouin, N., Quaas, J., Gryspeerdt, E., Kinne, S., Stier, P., Watson-Parris, D., Boucher, O., Carslaw, K. S., Christensen,
- 1426 M., Daniau, A.-L., Dufresne, J.-L., Feingold, G., Fiedler, S., Forster, P., Gettelman, A., Haywood, J. M., Lohmann, U.,
- 1427 Malavelle, F., Mauritsen, T., McCoy, D. T., Myhre, G., Mülmenstädt, J., Neubauer, D., Possner, A., Rugenstein, M., Sato,
- 1428 Y., Schulz, M., Schwartz, S. E., Sourdeval, O., Storelvmo, T., Toll, V., Winker, D., and Stevens, B.: Bounding Global
- e2019RG000660. 1429 Radiative Forcing of Climate Change, Rev. Geophys., 58.
- 1430 https://doi.org/10.1029/2019RG000660, 2020.
- 1431 Bergman, T., Kerminen, V. M., Korhonen, H., Lehtinen, K. J., Makkonen, R., Arola, A., Mielonen, T., Romakkaniemi,
- S., Kulmala, M., and Kokkola, H.: Evaluation of the sectional aerosol microphysics module SALSA implementation in 1432
- 1433 ECHAM5-HAM aerosol-climate model, Geosci. Model Dev., 5, 845-868, https://doi.org/10.5194/gmd-5-845-2012,
- 1434
- 1435 Blichner, S. M., Yli-Juuti, T., Mielonen, T., Pöhlker, C., Holopainen, E., Heikkinen, L., Mohr, C., Artaxo, P., Carbone,
- 1436 S., Meller, B. B., Quaresma Dias-Júnior, C., Kulmala, M., Petäjä, T., Scott, C. E., Svenhag, C., Nieradzik, L., Sporre, M., 1437
  - Partridge, D. G., Toyazzi, E., Virtanen, A., Kokkola, H., and Riipinen, I.: Process-evaluation of forest aerosol-cloud-
- 1438 climate feedback shows clear evidence from observations and large uncertainty in models, Nat. Commun., 15, 969,
- https://doi.org/10.1038/s41467-024-45001-y, 2024. 1439
- 1440 Boucher, O.: Climate Change 2013: The Physical Science Basis, edited by: Stoker, T. et al., Cambridge University Press,
- 1441 2013
- 1442 Browse, J., Carslaw, K. S., Mann, G. W., Birch, C. E., Arnold, S. R., and Leck, C.: The complex response of Arctic 1443
  - aerosol to sea-ice retreat, Atmospheric Chem. Phys., 14, 7543-7557, https://doi.org/10.5194/acp-14-7543-2014, 2014.
- 1444 Chim, M. M., Aubry, T. J., Abraham, N. L., Marshall, L., Mulcahy, J., Walton, J., and Schmidt, A.: Climate Projections
- Very Likely Underestimate Future Volcanic Forcing and Its Climatic Effects, Geophys. Res. Lett., 50, e2023GL103743, 1445
- 1446 https://doi.org/10.1029/2023GL103743, 2023.
- 1447 Cox, P.: Description of the "TRIFFID" DynamicGlobal Vegetation Model, 2001.
- Croft, B., Lohmann, U., Martin, R. V., Stier, P., Wurzler, S., Feichter, J., Posselt, R., and Ferrachat, S.; Aerosol size-1448
- dependent below-cloud scavenging by rain and snow in the ECHAM5-HAM, Atmospheric Chem. Phys., 9, 4653-4675, 1449
- 1450 https://doi.org/10.5194/acp-9-4653-2009, 2009.
- 1451 Croft, B., Lohmann, U., Martin, R. V., Stier, P., Wurzler, S., Feichter, J., Hoose, C., Heikkilä, U., van Donkelaar, A., and
- 1452 Ferrachat, S.: Influences of in-cloud aerosol scavenging parameterizations on aerosol concentrations and wet deposition
- 1453 in ECHAM5-HAM, Atmospheric Chem. Phys., 10, 1511-1543, https://doi.org/10.5194/acp-10-1511-2010, 2010.
- Dadashazar, H., Alipanah, M., Hilario, M. R. A., Crosbie, E., Kirschler, S., Liu, H., Moore, R. H., Peters, A. J., Scarino, 1454
- 1455 A. J., Shook, M., Thornhill, K. L., Voigt, C., Wang, H., Winstead, E., Zhang, B., Ziemba, L., and Sorooshian, A.: Aerosol

- 1456 responses to precipitation along North American air trajectories arriving at Bermuda, Atmospheric Chem. Phys., 21,
- 1457 16121-16141, https://doi.org/10.5194/acp-21-16121-2021, 2021.
- 1458 Dee, D. P., Uppala, S. M., Simmons, A. J., Berrisford, P., Poli, P., Kobayashi, S., Andrae, U., Balmaseda, M. A., Balsamo,
- 1459 G., Bauer, P., Bechtold, P., Beljaars, A. C. M., van de Berg, L., Bidlot, J., Bormann, N., Delsol, C., Dragani, R., Fuentes,
- 1460 M., Geer, A. J., Haimberger, L., Healy, S. B., Hersbach, H., Hólm, E. V., Isaksen, L., Kållberg, P., Köhler, M., Matricardi,
- 1461 M., McNally, A. P., Monge-Sanz, B. M., Morcrette, J.-J., Park, B.-K., Peubey, C., de Rosnay, P., Tavolato, C., Thépaut,
- 1462 J.-N., and Vitart, F.: The ERA-Interim reanalysis: configuration and performance of the data assimilation system, Q. J.
- 1463 R. Meteorol. Soc., 137, 553-597, https://doi.org/10.1002/qj.828, 2011.
- 1464 Draxler, R. R. and Hess, G. D.: An overview of the HYSPLIT\_4 modelling system for trajectories, dispersion and
- deposition, Aust. Meteorol. Mag., 47, 295-308, 1998. 1465
- 1466 Drinovec, L., Močnik, G., Zotter, P., Prévôt, A. S. H., Ruckstuhl, C., Coz, E., Rupakheti, M., Sciare, J., Müller, T.,
- Wiedensohler, A., and Hansen, A. D. A.: The "dual-spot" Aethalometer: an improved measurement of aerosol black 1467
- carbon with real-time loading compensation, Atmospheric Meas. Tech., 8, 1965-1979, https://doi.org/10.5194/amt-8-1468
- 1965-2015, 2015. 1469
- 1470 Durack, P. J., Taylor, K. E., Eyring, V., Ames, S. K., Hoang, A., and Doutriaux, C.: input4MIPs: Making model forcing
- 1471 more transparent, 2017.
- 1472 Dusek, U., Frank, G. P., Hildebrandt, L., Curtius, J., Schneider, J., Walter, S., Chand, D., Drewnick, F., Hings, S., Jung,
- 1473 D., Borrmann, S., and Andreae, M. O.: Size Matters More Than Chemistry for Cloud-Nucleating Ability of Aerosol
- 1474 Particles, Science, 312, 1375-1378, https://doi.org/10.1126/science.1125261, 2006.
- Ervens, B.: Modeling the Processing of Aerosol and Trace Gases in Clouds and Fogs, Chem. Rev., 115, 4157-4198, 1475
- 1476 https://doi.org/10.1021/cr5005887, 2015.
- 1477 Ervens, B., Sorooshian, A., Aldhaif, A. M., Shingler, T., Crosbie, E., Ziemba, L., Campuzano-Jost, P., Jimenez, J. L., and
- 1478 Wisthaler, A.: Is there an aerosol signature of chemical cloud processing?, Atmospheric Chem. Phys., 18, 16099-16119, 1479
  - https://doi.org/10.5194/acp-18-16099-2018, 2018.
- 1480 Eyring, V., Bony, S., Meehl, G. A., Senior, C. A., Stevens, B., Stouffer, R. J., and Taylor, K. E.: Overview of the Coupled
- 1481 Model Intercomparison Project Phase 6 (CMIP6) experimental design and organization, Geosci. Model Dev., 9, 1937-
- 1482 1958, https://doi.org/10.5194/gmd-9-1937-2016, 2016.
- 1483 Forster, P., Storelvmo, T., Armour, K., Collins, W., Dufresne, J.-L., Frame, D., Lunt, D. J., Mauritsen, T., Palmer, M. D.,
- 1484 Watanabe, M., Wild, M., and Zhang, H.: The Earth's Energy Budget, Climate Feedbacks and Climate Sensitivity, in:
- 1485 Climate Change 2021 - The Physical Science Basis: Working Group I Contribution to the Sixth Assessment Report of 1486
  - the Intergovernmental Panel on Climate Change, edited by: Masson-Delmotte, V., Zhai, P., Pirani, A., Connors, S. L.,
- 1487 Péan, C., Berger, S., Caud, N., Chen, Y., Goldfarb, L., Gormis, M. I., Huang, M., Leitzell, K., Lonnoy, E., Matthews, J.
- 1488 B. R., Maycock, T. K., Waterfield, T., Yelekçi, O., Yu, R., and Zhou, B., Cambridge University Press, Cambridge, 923-
- 1054, https://doi.org/10.1017/9781009157896.009, 2021. 1489
- 1490 Franco, M. A., Ditas, F., Kremper, L. A., Machado, L. A. T., Andreae, M. O., Araújo, A., Barbosa, H. M. J., de Brito, J.
- F., Carbone, S., Holanda, B. A., Morais, F. G., Nascimento, J. P., Pöhlker, M. L., Rizzo, L. V., Sá, M., Saturno, J., Walter, 1491
- 1492 D., Wolff, S., Pöschl, U., Artaxo, P., and Pöhlker, C.: Occurrence and growth of sub-50 nm aerosol particles in the 1493
  - Amazonian boundary layer, Atmospheric Chem. Phys., 22, 3469–3492, https://doi.org/10.5194/acp-22-3469-2022, 2022.
- 1494 Gilardoni, S., Massoli, P., Paglione, M., Giulianelli, L., Carbone, C., Rinaldi, M., Decesari, S., Sandrini, S., Costabile, F.,
- 1495 Gobbi, G. P., Pietrogrande, M. C., Visentin, M., Scotto, F., Fuzzi, S., and Facchini, M. C.: Direct observation of aqueous 1496 secondary organic aerosol from biomass-burning emissions, Proc. Natl. Acad. Sci., 113, 10013-10018,
- https://doi.org/10.1073/pnas.1602212113, 2016. 1497
- 1498 Gliß, J., Mortier, A., Schulz, M., Andrews, E., Balkanski, Y., Bauer, S. E., Benedictow, A. M. K., Bian, H., Checa-Garcia,
- 1499 R., Chin, M., Ginoux, P., Griesfeller, J. J., Heckel, A., Kipling, Z., Kirkevåg, A., Kokkola, H., Laj, P., Le Sager, P., Lund,
- 1500 M. T., Lund Myhre, C., Matsui, H., Myhre, G., Neubauer, D., van Noije, T., North, P., Olivié, D. J. L., Rémy, S., 1501 Sogacheva, L., Takemura, T., Tsigaridis, K., and Tsyro, S. G.: AeroCom phase III multi-model evaluation of the aerosol
- 1502 life cycle and optical properties using ground- and space-based remote sensing as well as surface in situ observations,
- 1503 Atmospheric Chem. Phys., 21, 87–128, https://doi.org/10.5194/acp-21-87-2021, 2021.

- 1504 Graham, E. L., Zieger, P., Mohr, C., Wideqvist, U., Hennig, T., Ekman, A. M. L., Krejci, R., Ström, J., and Riipinen, I.:
- 1505 Physical and chemical properties of aerosol particles and cloud residuals on Mt. Åreskutan in Central Sweden during
- 1506 summer 2014, 72, 1776080, https://doi.org/10.1080/16000889.2020.1776080, 2020.
- Häkkinen, S. A. K., Äijälä, M., Lehtipalo, K., Junninen, H., Backman, J., Virkkula, A., Nieminen, T., Vestenius, M., 1507
- 1508 Hakola, H., Ehn, M., Worsnop, D. R., Kulmala, M., Petäjä, T., and Riipinen, I.: Long-term volatility measurements of
- 1509 submicron atmospheric aerosol in Hyytiälä, Finland, Atmos Chem Phys, 12, 10771-10786, https://doi.org/10.5194/acp-
- 1510 12-10771-2012, 2012.
- 1511 Hardacre, C., Mulcahy, J. P., Pope, R. J., Jones, C. G., Rumbold, S. T., Li, C., Johnson, C., and Turnock, S. T.: Evaluation
- of SO2, SO42- and an updated SO2 dry deposition parameterization in the United Kingdom Earth System Model, Atmos 1512
  - Chem Phys, 21, 18465–18497, https://doi.org/10.5194/acp-21-18465-2021, 2021.
- 1514 Hari, P. and Kulmala, M.: Station for measuring ecosystem-atmosphere relations (SMEAR II), Boreal Environ. Res., 10,
- 1515 315-322, 2005.

- Hartigan, J. A. and Wong, M. A.: Algorithm AS 136: A K-Means Clustering Algorithm, J. R. Stat. Soc. Ser. C Appl. 1516
- 1517 Stat., 28, 100-108, https://doi.org/10.2307/2346830, 1979.
- Heikkinen, L., Äijälä, M., Riva, M., Luoma, K., Dällenbach, K., Aalto, J., Aalto, P., Aliaga, D., Aurela, M., Keskinen, 1518
- 1519 H., Makkonen, U., Rantala, P., Kulmala, M., Petäjä, T., Worsnop, D., and Ehn, M.: Long-term sub-micrometer aerosol
- 1520 chemical composition in the boreal forest: inter- and intra-annual variability, Atmos Chem Phys, 20, 3151-3180,
- 1521 https://doi.org/10.5194/acp-20-3151-2020, 2020.
- 1522 Heslin-Rees, D., Tunved, P., Ström, J., Cremer, R., Zieger, P., Riipinen, I., Ekman, A. M. L., Eleftheriadis, K., and Krejci,
- 1523 R.: Increase in precipitation scavenging contributes to long-term reductions of light-absorbing aerosol in the Arctic,
- Atmospheric Chem. Phys., 24, 2059–2075, https://doi.org/10.5194/acp-24-2059-2024, 2024. 1524
- 1525 Hewitt, H. T., Copsey, D., Culverwell, I. D., Harris, C. M., Hill, R. S. R., Keen, A. B., McLaren, A. J., and Hunke, E. C.:
- 1526 Design and implementation of the infrastructure of HadGEM3: the next-generation Met Office climate modelling system, 1527
  - Geosci. Model Dev., 4, 223–253, https://doi.org/10.5194/gmd-4-223-2011, 2011.
- 1528 Holopainen, E., Kokkola, H., Laakso, A., and Kühn, T.: In-cloud scavenging scheme for sectional aerosol modules -
- 1529 implementation in the framework of the Sectional Aerosol module for Large Scale Applications version 2.0 (SALSA2.0)
- 1530 global aerosol module, Geosci Model Dev, 13, 6215–6235, https://doi.org/10.5194/gmd-13-6215-2020, 2020.
- 1531 Huang, L., An, J., Koo, B., Yarwood, G., Yan, R., Wang, Y., Huang, C., and Li, L.: Sulfate formation during heavy winter
- 1532 haze events and the potential contribution from heterogeneous SO2 + NO2 reactions in the Yangtze River Delta region,
- 1533 China, Atmospheric Chem. Phys., 19, 14311-14328, https://doi.org/10.5194/acp-19-14311-2019, 2019.
- 1534 Isokääntä, S., Kim, P., Mikkonen, S., Kühn, T., Kokkola, H., Yli-Juuti, T., Heikkinen, L., Luoma, K., Petäjä, T., Kipling,
- 1535 Z., Partridge, D., and Virtanen, A.: The effect of clouds and precipitation on the aerosol concentrations and composition
- 1536 in a boreal forest environment, Atmospheric Chem. Phys., 22, 11823-11843, https://doi.org/10.5194/acp-22-11823-2022,
- 1537
- 1538 Jordan, G., Haywood, J., Malavelle, F., Chen, Y., Peace, A., Duncan, E., Partridge, D. G., Kim, P., Watson-Parris, D.,
- 1539 Takemura, T., Neubauer, D., Myhre, G., Skeie, R., and Laakso, A.: How well are aerosol-cloud interactions represented
- in climate models? Part 1: Understanding the sulphate aerosol production from the 2014–15 Holuhraun eruption, EGUsphere, 2023, 1–34, https://doi.org/10.5194/egusphere-2023-619, 2023. 1540
- 1541
- 1542 Kesti, J., Asmi, E., O'Connor, E. J., Backman, J., Budhavant, K., Andersson, A., Dasari, S., Praveen, P. S., Zahid, H.,
- 1543 and Gustafsson, Ö.: Changes in aerosol size distributions over the Indian Ocean during different meteorological
- 1544
- 1545 Khadir, T., Riipinen, I., Talvinen, S., Heslin-Rees, D., Pöhlker, C., Rizzo, L., Machado, L. A. T., Franco, M. A., Kremper,
- 1546 L. A., Artaxo, P., Petäjä, T., Kulmala, M., Tunved, P., Ekman, A. M. L., Krejci, R., and Virtanen, A.: Sink, Source or
- 1547 Something In-Between? Net Effects of Precipitation on Aerosol Particle Populations, Geophys. Res. Lett., 50,
- e2023GL104325, https://doi.org/10.1029/2023GL104325, 2023. 1548

- 1549 Kim, P., Partridge, D., and Haywood, J.: Constraining the model representation of the aerosol life cycle in relation to
- 1550 sources and sinks., Copernicus Meetings, https://doi.org/10.5194/egusphere-egu2020-21948, 2020.
- 1551 Kipling, Z., Stier, P., Schwarz, J. P., Perring, A. E., Spackman, J. R., Mann, G. W., Johnson, C. E., and Telford, P. J.:
- 1552 Constraints on aerosol processes in climate models from vertically-resolved aircraft observations of black carbon, Atmos
- 1553 Chem Phys, 13, 5969–5986, https://doi.org/10.5194/acp-13-5969-2013, 2013.
- 1554 Kokkola, H., Kühn, T., Laakso, A., Bergman, T., Lehtinen, K. E. J., Mielonen, T., Arola, A., Stadtler, S., Korhonen, H.,
- 1555 Ferrachat, S., Lohmann, U., Neubauer, D., Tegen, I., Siegenthaler-Le Drian, C., Schultz, M. G., Bey, I., Stier, P.,
- 1556 Daskalakis, N., Heald, C. L., and Romakkaniemi, S.: SALSA2.0: The sectional aerosol module of the aerosol-chemistry-
- 1557 climate model ECHAM6.3.0-HAM2.3-MOZ1.0, Geosci Model Dev, 11, 3833-3863, https://doi.org/10.5194/gmd-11-
- 1558 3833-2018, 2018,
- 1559 Kulmala, M., Rannik, Ü., Pirjola, L., Dal Maso, M., Karimäki, J., Asmi, A., Jäppinen, A., Karhu, V., Korhonen, H.,
- 1560 Malvikko, S.-P., Raittila, J., Šuni, T., Yli-Koivisto, S., and Vesala, T.: Characterization of atmospheric trace gas and
- 1561 aerosol concentrations at forest sites in southern and northern Finland using back trajectories, Boreal Environ. Res. Int.
- Interdiscip. J., 315-336, 2000. 1562
- 1563 Laakso, A., Niemeier, U., Visioni, D., Tilmes, S., and Kokkola, H.: Dependency of the impacts of geoengineering on the
- 1564 stratospheric sulfur injection strategy - Part 1: Intercomparison of modal and sectional aerosol modules, Atmos Chem
- Phys, 22, 93–118, https://doi.org/10.5194/acp-22-93-2022, 2022. 1565
- 1566 Labe, Z. M. and Barnes, E. A.: Comparison of Climate Model Large Ensembles With Observations in the Arctic Using
- 1567 Simple Neural Networks, Earth Space Sci., 9, e2022EA002348, https://doi.org/10.1029/2022EA002348, 2022.
- 1568 Lamkaddam, H., Dommen, J., Ranjithkumar, A., Gordon, H., Wehrle, G., Krechmer, J., Majluf, F., Salionov, D., Schmale,
- J., Bjelic, S., Carslaw, K. S., El Haddad, I., and Baltensperger, U.: Large contribution to secondary organic aerosol from 1569
- isoprene cloud chemistry, Sci. Adv., 7, https://doi.org/10.1126/sciadv.abe2952, 2021. 1570
- 1571 Liao, L., Dal Maso, M., Taipale, R., Rinne, J., Ehn, M., Junninen, H., Aijala, M., Nieminen, T., Alekseychik, P.,
- Hulkkonen, M., Worsnop, D. R., Kerminen, V. M., and Kulmala, M.: Monoterpene pollution episodes in a forest 1572
- 1573 environment: indication of anthropogenic origin and association with aerosol particles, Boreal Environ. Res., 16, 288-
- 1574 303, 2011.
- 1575 Liu, D., He, C., Schwarz, J. P., and Wang, X.: Lifecycle of light-absorbing carbonaceous aerosols in the atmosphere, Npj
- 1576 Clim. Atmospheric Sci., 3, 40, https://doi.org/10.1038/s41612-020-00145-8, 2020a.
- 1577 Liu, P., Ye, C., Xue, C., Zhang, C., Mu, Y., and Sun, X.: Formation mechanisms of atmospheric nitrate and sulfate during
- 1578 the winter haze pollution periods in Beijing: gas-phase, heterogeneous and aqueous-phase chemistry, Atmospheric Chem.
- 1579 Phys., 20, 4153-4165, https://doi.org/10.5194/acp-20-4153-2020, 2020b.
- 1580 Liu, P. S. K., Deng, R., Smith, K. A., Williams, L. R., Jayne, J. T., Canagaratna, M. R., Moore, K., Onasch, T. B.,
- 1581 Worsnop, D. R., and Deshler, T.: Transmission Efficiency of an Aerodynamic Focusing Lens System: Comparison of
- 1582 Model Calculations and Laboratory Measurements for the Aerodyne Aerosol Mass Spectrometer, Aerosol Sci. Technol.,
- 41, 721-733, https://doi.org/10.1080/02786820701422278, 2007. 1583
- 1584 Luoma, K., Virkkula, A., Aalto, P., Petäjä, T., and Kulmala, M.: Over a 10-year record of aerosol optical properties at
- SMEAR II, Atmospheric Chem. Phys., 19, 11363–11382, https://doi.org/10.5194/acp-19-11363-2019, 2019. 1585
- 1586 Machado, L. A. T., Franco, M. A., Kremper, L. A., Ditas, F., Andreae, M. O., Artaxo, P., Cecchini, M. A., Holanda, B.
- A., Pöhlker, M. L., Saraiva, I., Wolff, S., Pöschl, U., and Pöhlker, C.: How weather events modify aerosol particle size 1587
- 1588 distributions in the Amazon boundary layer, Atmospheric Chem. Phys., 21, 18065-18086, https://doi.org/10.5194/acp-
- 1589 21-18065-2021, 2021.
- 1590 Maher, N., Power, S. B., and Marotzke, J.: More accurate quantification of model-to-model agreement in externally forced
- 1591 climatic responses over the coming century, Nat. Commun., 12, 788, https://doi.org/10.1038/s41467-020-20635-w, 2021.
- 1592 Mann, G. W., Carslaw, K. S., Spracklen, D. V., Ridley, D. A., Manktelow, P. T., Chipperfield, M. P., Pickering, S. J., 1593 and Johnson, C. E.: Description and evaluation of GLOMAP-mode: a modal global aerosol microphysics model for the
- 1594 UKCA composition-climate model, Geosci Model Dev, 3, 519-551, https://doi.org/10.5194/gmd-3-519-2010, 2010.

- 1595 Mann, G. W., Carslaw, K. S., Ridley, D. A., Spracklen, D. V., Pringle, K. J., Merikanto, J., Korhonen, H., Schwarz, J. P.,
- 1596 Lee, L. A., Manktelow, P. T., Woodhouse, M. T., Schmidt, A., Breider, T. J., Emmerson, K. M., Reddington, C. L.,
- 1597 Chipperfield, M. P., and Pickering, S. J.: Intercomparison of modal and sectional aerosol microphysics representations
- 1598 within the same 3-D global chemical transport model, Atmos Chem Phys, 12, 4449-4476, https://doi.org/10.5194/acp-
- 1599 12-4449-2012, 2012.
- 1600 McCoy, I. L., Bretherton, C. S., Wood, R., Twohy, C. H., Gettelman, A., Bardeen, C. G., and Toohey, D. W.: Influences
- 1601 of Recent Particle Formation on Southern Ocean Aerosol Variability and Low Cloud Properties, J. Geophys. Res. 1602
  - Atmospheres, 126, e2020JD033529, https://doi.org/10.1029/2020JD033529, 2021.
- 1603 Morgenstern, O., Braesicke, P., O'Connor, F. M., Bushell, A. C., Johnson, C. E., Osprey, S. M., and Pyle, J. A.: Evaluation
- 1604 of the new UKCA climate-composition model - Part 1: The stratosphere, Geosci. Model Dev., 2, 43-57,
- https://doi.org/10.5194/gmd-2-43-2009, 2009. 1605
- 1606 Mulcahy, J. P., Johnson, C., Jones, C. G., Povey, A. C., Scott, C. E., Sellar, A., Turnock, S. T., Woodhouse, M. T.,
- 1607 Abraham, N. L., Andrews, M. B., Bellouin, N., Browse, J., Carslaw, K. S., Dalvi, M., Folberth, G. A., Glover, M.,
- 1608 Grosvenor, D. P., Hardacre, C., Hill, R., Johnson, B., Jones, A., Kipling, Z., Mann, G., Mollard, J., O'Connor, F. M.,
- Palmiéri, J., Reddington, C., Rumbold, S. T., Richardson, M., Schutgens, N. A. J., Stier, P., Stringer, M., Tang, Y., 1609
- 1610 Walton, J., Woodward, S., and Yool, A.: Description and evaluation of aerosol in UKESM1 and HadGEM3-GC3.1
- CMIP6 historical simulations, Geosci Model Dev, 13, 6383-6423, https://doi.org/10.5194/gmd-13-6383-2020, 2020. 1611
- Ng, N. L., Herndon, S. C., Trimborn, A., Canagaratna, M. R., Croteau, P. L., Onasch, T. B., Sueper, D., Worsnop, D. R., 1612
- 1613 Zhang, Q., Sun, Y. L., and Jayne, J. T.: An Aerosol Chemical Speciation Monitor (ACSM) for Routine Monitoring of the
- 1614 Composition and Mass Concentrations of Ambient Aerosol, Aerosol Sci. Technol., 45, 780-794,
- 1615 https://doi.org/10.1080/02786826.2011.560211, 2011.
- 1616 Nieminen, T., Asmi, A., Dal Maso, M., Aalto, P. P., Keronen, P., Petaja, T., Kulmala, M., and Kerminen, V. M.: Trends
- 1617 in atmospheric new-particle formation: 16 years of observations in a boreal-forest environment, Boreal Environ. Res., 19,
- 191-214, 2014. 1618
- O'Connor, F. M., Johnson, C. E., Morgenstern, O., Abraham, N. L., Braesicke, P., Dalvi, M., Folberth, G. A., Sanderson,
- 1620 M. G., Telford, P. J., Voulgarakis, A., Young, P. J., Zeng, G., Collins, W. J., and Pyle, J. A.: Evaluation of the new UKCA 1621
  - climate-composition model Part 2: The Troposphere, Geosci. Model Dev., 7, 41-91, https://doi.org/10.5194/gmd-7-41-91
- 2014 2014 1622
- 1623 Ohata, S., Moteki, N., Mori, T., Koike, M., and Kondo, Y.: A key process controlling the wet removal of aerosols: new
- observational evidence, Sci. Rep., 6, 34113, https://doi.org/10.1038/srep34113, 2016. 1624
- 1625 Partridge, D. G., Vrugt, J. A., Tunved, P., Ekman, A. M. L., Struthers, H., and Sorooshian, A.: Inverse modelling of cloud-
- 1626 aerosol interactions - Part 2: Sensitivity tests on liquid phase clouds using a Markov chain Monte Carlo based simulation
- 1627 approach, Atmospheric Chem. Phys., 12, 2823-2847, https://doi.org/10.5194/acp-12-2823-2012, 2012.
- 1628 Pathak, R., Dasari, H. P., Ashok, K., and Hoteit, I.: Effects of multi-observations uncertainty and models similarity on
- climate change projections, Npj Clim. Atmospheric Sci., 6, 1-12, https://doi.org/10.1038/s41612-023-00473-5, 2023. 1629
- 1630 Petäjä, T., Tabakova, K., Manninen, A., Ezhova, E., O'Connor, E., Moisseev, D., Sinclair, V. A., Backman, J., Levula,
- 1631 J., Luoma, K., Virkkula, A., Paramonov, M., Räty, M., Äijälä, M., Heikkinen, L., Ehn, M., Sipilä, M., Yli-Juuti, T.,
- Virtanen, A., Ritsche, M., Hickmon, N., Pulik, G., Rosenfeld, D., Worsnop, D. R., Bäck, J., Kulmala, M., and Kerminen, 1632
- 1633 V. M.: Influence of biogenic emissions from boreal forests on aerosol-cloud interactions, Nat. Geosci., 15, 42-47,
- https://doi.org/10.1038/s41561-021-00876-0, 2022. 1634
- 1635 Quaas, J., Jia, H., Smith, C., Albright, A. L., Aas, W., Bellouin, N., Boucher, O., Doutriaux-Boucher, M., Forster, P. M.,
- Grosvenor, D., Jenkins, S., Klimont, Z., Loeb, N. G., Ma, X., Naik, V., Paulot, F., Stier, P., Wild, M., Myhre, G., and 1636
- Schulz, M.: Robust evidence for reversal of the trend in aerosol effective climate forcing, Atmospheric Chem. Phys., 22, 1637 1638
  - 12221-12239, https://doi.org/10.5194/acp-22-12221-2022, 2022.
- 1639 R Core Team: R: A language and environment for statistical computing, R Found. Stat. Comput., 2024.

- Reddington, C. L., Spracklen, D. V., Artaxo, P., Ridley, D. A., Rizzo, L. V., and Arana, A.: Analysis of particulate 1640
- 1641 emissions from tropical biomass burning using a global aerosol model and long-term surface observations, Atmospheric
- 1642 Chem. Phys., 16, 11083–11106, https://doi.org/10.5194/acp-16-11083-2016, 2016.
- 1643 Reutter, P., Su. H., Trentmann, J., Simmel, M., Rose, D., Gunthe, S. S., Wernli, H., Andreae, M. O., and Pöschl, U.:
- 1644 Aerosol- and updraft-limited regimes of cloud droplet formation: influence of particle number, size and hygroscopicity
- 1645 on the activation of cloud condensation nuclei (CCN), Atmospheric Chem. Phys., 9,
- https://doi.org/10.5194/acp-9-7067-2009, 2009. 1646
- 1647 Riuttanen, L., Hulkkonen, M., Dal Maso, M., Junninen, H., and Kulmala, M.: Trajectory analysis of atmospheric transport
- of fine particles, SO2, NOx and O3 to the SMEAR II station in Finland in 1996-2008, Atmospheric Chem. Phys., 13, 1648
- 1649 2153-2164, https://doi.org/10.5194/acp-13-2153-2013, 2013.
- 1650 Schultz, M. G., Stadtler, S., Schröder, S., Taraborrelli, D., Franco, B., Krefting, J., Henrot, A., Ferrachat, S., Lohmann,
- U., Neubauer, D., Siegenthaler-Le Drian, C., Wahl, S., Kokkola, H., Kühn, T., Rast, S., Schmidt, H., Stier, P., Kinnison, 1651
- 1652 D., Tyndall, G. S., Orlando, J. J., and Wespes, C.: The chemistry-climate model ECHAM6.3-HAM2.3-MOZ1.0, Geosci
- Model Dev, 11, 1695–1723, https://doi.org/10.5194/gmd-11-1695-2018, 2018. 1653
- 1654 Schumacher, C. and Funk, A.: Assessing Convective-Stratiform Precipitation Regimes in the Tropics and Extratropics
- With the GPM Satellite Radar, Geophys. Res. Lett., 50, e2023GL102786, https://doi.org/10.1029/2023GL102786, 2023. 1655
- 1656 Schutgens, N. A. J., Partridge, D. G., and Stier, P.: The importance of temporal collocation for the evaluation of aerosol
- 1657 models with observations, Atmos Chem Phys, 16, 1065-1079, https://doi.org/10.5194/acp-16-1065-2016, 2016.
- 1658 Seinfeld, J. H. and Pandis, S. N.: Atmospheric chemistry and physics: from air pollution to climate change, Third edition.,
- 1659 John Wiley & Sons, Inc., Hoboken, New Jersey, 2016.
- 1660 Sellar, A. A., Jones, C. G., Mulcahy, J. P., Tang, Y., Yool, A., Wiltshire, A., O'Connor, F. M., Stringer, M., Hill, R.,
- Palmieri, J., Woodward, S., de Mora, L., Kuhlbrodt, T., Rumbold, S. T., Kelley, D. I., Ellis, R., Johnson, C. E., Walton, 1661 1662 J., Abraham, N. L., Andrews, M. B., Andrews, T., Archibald, A. T., Berthou, S., Burke, E., Blockley, E., Carslaw, K.,
- Dalvi, M., Edwards, J., Folberth, G. A., Gedney, N., Griffiths, P. T., Harper, A. B., Hendry, M. A., Hewitt, A. J., Johnson, 1663
- B., Jones, A., Jones, C. D., Keeble, J., Liddicoat, S., Morgenstern, O., Parker, R. J., Predoi, V., Robertson, E., Siahaan, 1664
- 1665 A., Smith, R. S., Swaminathan, R., Woodhouse, M. T., Zeng, G., and Zerroukat, M.: UKESM1: Description and
- 1666 Evaluation of the U.K. Earth System Model, J. Adv. Model. Earth Syst., 11, 4513-4558,
- https://doi.org/10.1029/2019MS001739, 2019. 1667
- 1668 Stein, A. F., Draxler, R. R., Rolph, G. D., Stunder, B. J. B., Cohen, M. D., and Ngan, F.: Noaa's Hysplit Atmospheric
- 1669 Transport and Dispersion Modeling System, Bull. Am. Meteorol. Soc., 96, 2059–2077, https://doi.org/10.1175/Bams-D-
- 1670 14-00110.1, 2015.
- 1671 Stevens, B., Giorgetta, M., Esch, M., Mauritsen, T., Crueger, T., Rast, S., Salzmann, M., Schmidt, H., Bader, J., Block,
- 1672 K., Brokopf, R., Fast, I., Kinne, S., Kornblueh, L., Lohmann, U., Pincus, R., Reichler, T., and Roeckner, E.: Atmospheric 1673
  - component of the MPI-M Earth System Model: ECHAM6, J. Adv. Model. Earth Syst., 5, 146-172,
- 1674 https://doi.org/10.1002/jame.20015, 2013.
- Stier, P., Feichter, J., Kinne, S., Kloster, S., Vignati, E., Wilson, J., Ganzeveld, L., Tegen, I., Werner, M., Balkanski, Y., 1675
- 1676 Schulz, M., Boucher, O., Minikin, A., and Petzold, A.: The aerosol-climate model ECHAM5-HAM, Atmos Chem Phys,
- 5, 1125-1156, https://doi.org/10.5194/acp-5-1125-2005, 2005. 1677
- 1678 Talvinen, S., Kim, P., Tovazzi, E., Holopainen, E., Cremer, R., Kühn, T., Kokkola, H., Kipling, Z., Neubauer, D.,
- 1679 Teixeira, J. C., Sellar, A., Watson-Parris, D., Yang, Y., Zhu, J., Krishnan, S., Virtanen, A., and Partridge, D. G.: Codes 1680
- for "Towards an improved understanding of the impact of clouds and precipitation on the representation of aerosols over the Boreal Forest in GCMs" by Talvinen et al., , https://doi.org/10.5281/zenodo.16902872, 2025a. 1681
- 1682 Talvinen, S., Kim, P., Tovazzi, E., Holopainen, E., Cremer, R., Kühn, T., Kokkola, H., Kipling, Z., Neubauer, D.,
- Teixeira, J. C., Sellar, A., Watson-Parris, D., Yang, Y., Zhu, J., Krishnan, S., Virtanen, A., and Partridge, D. G.: Data for 1683
- 1684 "Towards an improved understanding of the impact of clouds and precipitation on the representation of aerosols over the
- 1685 Boreal Forest in GCMs" by Talvinen et al., 2025b.

- 1686 Tegen, I., Neubauer, D., Ferrachat, S., Siegenthaler-Le Drian, C., Bey, I., Schutgens, N., Stier, P., Watson-Parris, D.,
- Stanelle, T., Schmidt, H., Rast, S., Kokkola, H., Schultz, M., Schroeder, S., Daskalakis, N., Barthel, S., Heinold, B., and Lohmann, U.: The global aerosol–climate model ECHAM6.3–HAM2.3 Part 1: Aerosol evaluation, Geosci Model Dev, 1687
- 1688
- 12, 1643-1677, https://doi.org/10.5194/gmd-12-1643-2019, 2019. 1689
- 1690 Telford, P. J., Braesicke, P., Morgenstern, O., and Pyle, J. A.: Technical Note: Description and assessment of a nudged
- 1691 version of the new dynamics Unified Model, Atmos Chem Phys, 8, 1701-1712, https://doi.org/10.5194/acp-8-1701-2008,
- 1692

1695

- 1693 Textor, C., Schulz, M., Guibert, S., Kinne, S., Balkanski, Y., Bauer, S., Berntsen, T., Berglen, T., Boucher, O., Chin, M.,
- Dentener, F., Diehl, T., Easter, R., Feichter, H., Fillmore, D., Ghan, S., Ginoux, P., Gong, S., Kristjansson, J. E., Krol, 1694
  - M., Lauer, A., Lamarque, J. F., Liu, X., Montanaro, V., Myhre, G., Penner, J., Pitari, G., Reddy, S., Seland, O., Stier, P.,
- 1696 Takemura, T., and Tie, X.: Analysis and quantification of the diversities of aerosol life cycles within AeroCom,
  - Atmospheric Chem. Phys., 6, 1777-1813, https://doi.org/10.5194/acp-6-1777-2006, 2006.
- 1698 Tunved, P. and Ström, J.: On the seasonal variation in observed size distributions in northern Europe and their changes
- 1699 with decreasing anthropogenic emissions in Europe: climatology and trend analysis based on 17 years of data from
- Aspyreten, Sweden, Atmospheric Chem. Phys., 19, 14849–14873, https://doi.org/10.5194/acp-19-14849-2019, 2019. 1700
- 1701 Tunved, P., Ström, J., and Hansson, H. C.: An investigation of processes controlling the evolution of the boundary layer
- 1702 aerosol size distribution properties at the Swedish background station Aspvreten, Atmospheric Chem. Phys., 4, 2581-
- 1703 2592, https://doi.org/10.5194/acp-4-2581-2004, 2004.
- 1704 Tunved, P., Ström, J., and Krejci, R.: Arctic aerosol life cycle: linking aerosol size distributions observed between 2000
- 1705 and 2010 with air mass transport and precipitation at Zeppelin station, Ny-Ålesund, Svalbard, Atmospheric Chem. Phys.,
- 1706 13, 3643-3660, https://doi.org/10.5194/acp-13-3643-2013, 2013.
- 1707 Walters, D., Baran, A. J., Boutle, I., Brooks, M., Earnshaw, P., Edwards, J., Furtado, K., Hill, P., Lock, A., Manners, J.,
- Morcrette, C., Mulcahy, J., Sanchez, C., Smith, C., Stratton, R., Tennant, W., Tomassini, L., Van Weverberg, K., Vosper, 1708
- 1709 S., Willett, M., Browse, J., Bushell, A., Carslaw, K., Dalvi, M., Essery, R., Gedney, N., Hardiman, S., Johnson, B., Johnson, C., Jones, A., Jones, C., Mann, G., Milton, S., Rumbold, H., Sellar, A., Ujiie, M., Whitall, M., Williams, K., and 1710
- 1711 Zerroukat, M.: The Met Office Unified Model Global Atmosphere 7.0/7.1 and JULES Global Land 7.0 configurations,
- 1712 Geosci. Model Dev., 12, 1909-1963, https://doi.org/10.5194/gmd-12-1909-2019, 2019.
- 1713 Wang, T., Li, K., Bell, D. M., Zhang, J., Cui, T., Surdu, M., Baltensperger, U., Slowik, J. G., Lamkaddam, H., El Haddad,
- I., and Prevot, A. S. H.: Large contribution of in-cloud production of secondary organic aerosol from biomass burning 1714
- emissions, Npj Clim. Atmospheric Sci., 7, 1-9, https://doi.org/10.1038/s41612-024-00682-6, 2024. 1715
- 1716 Wang, Y., Xia, W., and Zhang, G. J.: What rainfall rates are most important to wet removal of different aerosol types?,
- 1717 Atmospheric Chem. Phys., 21, 16797–16816, https://doi.org/10.5194/acp-21-16797-2021, 2021.
- 1718 Watson-Parris, D., Schutgens, N., Cook, N., Kipling, Z., Kershaw, P., Gryspeerdt, E., Lawrence, B., and Stier, P.:
- 1719 Community Intercomparison Suite (CIS) v1.4.0: a tool for intercomparing models and observations, Geosci. Model Dev.,
- 1720 9, 3093-3110, https://doi.org/10.5194/gmd-9-3093-2016, 2016.
- Watson-Parris, D., Schutgens, N., Reddington, C., Pringle, K. J., Liu, D., Allan, J. D., Coe, H., Carslaw, K. S., and Stier, 1721
- 1722 P.: In situ constraints on the vertical distribution of global aerosol, Atmos Chem Phys, 19, 11765-11790,
- 1723 https://doi.org/10.5194/acp-19-11765-2019, 2019.
- 1724 Williamson, C. J., Kupc, A., Axisa, D., Bilsback, K. R., Bui, T., Campuzano-Jost, P., Dollner, M., Froyd, K. D., Hodshire,
- A. L., Jimenez, J. L., Kodros, J. K., Luo, G., Murphy, D. M., Nault, B. A., Ray, E. A., Weinzierl, B., Wilson, J. C., Yu, 1725 1726
  - F., Yu. P., Pierce, J. R., and Brock, C. A.; A large source of cloud condensation nuclei from new particle formation in the
- tropics, Nature, 574, 399-403, https://doi.org/10.1038/s41586-019-1638-9, 2019. 1727
- 1728 Zhang, K., Wan, H., Liu, X., Ghan, S. J., Kooperman, G. J., Ma, P. L., Rasch, P. J., Neubauer, D., and Lohmann, U.:
- 1729 Technical Note: On the use of nudging for aerosol-climate model intercomparison studies, Atmos Chem Phys, 14, 8631-
  - 8645, https://doi.org/10.5194/acp-14-8631-2014, 2014.